MUON SPIN ROTATION/RELAXATION/RESONANCE

JESS H. BREWER *Canadian Institute of Advanced Research and Department of Physics, University of British Columbia, Vancouver, B.C., Canada V6T 1Z1*

In the past few decades, muon spin rotation/relaxation/resonance ($\mu\mathcal{SR}$) has become an indispensible experimental tool of condensed matter physics, chemistry and other material science as well as atomic, subatomic and other fundamental physics disciplines. This article outlines the history of $\mu\mathcal{SR}$, the basic muon physics that makes it possible, the principal $\mu\mathcal{SR}$ techniques and their main areas of application as of 1993.

INTRODUCTION

The acronyn "$\mu\mathcal{SR}$" was coined in 1974 (Newsletter, 1974); the definition and explanation offered on that occasion are still apt:

$\mu\mathcal{SR}$ stands for Muon Spin Relaxation, Rotation, Resonance, Research or what have you. The intention of the mnemonic acronym is to draw attention to the analogy with NMR and ESR, the range of whose applications is well known. Any study of the interactions of the muon spin by virtue of the asymmetric decay is considered $\mu\mathcal{SR}$, but this definition is not intended to exclude any peripherally related phenomena, especially if relevant to the use of the muon's magnetic moment as a delicate probe of matter.

Although muons were used as probes of magnetism in matter as early as 1944 (Rasetti, 1944), the essential property of the weak interaction that makes $\mu\mathcal{SR}$ possible — violation of parity ($\mathcal{P}$) symmetry — was posited by Lee and Yang in 1956 (Lee and Yang, 1956) to explain anomalies in kaon decay experiments (Fitch, 1981; Cronin, 1981). Of the famous measurements (Garwin *et al.*, 1957; Friedman and Telegdi, 1957; Wu *et al.*, 1957) confirming their hypothesis (Lee and Yang, 1957), one also suggested that $\mathcal{P}$-nonconservation in $\pi \rightarrow \mu \rightarrow e$ decay might furnish a sensitive general-purpose probe of matter. The history of $\mu\mathcal{SR}$ began with that experiment (Garwin *et al.*, 1957), which used an experimental method similar to the most common and familiar of modern $\mu\mathcal{SR}$ techniques: transverse field (TF)-$\mu\mathcal{SR}$.

Later sections will treat TF-$\mu\mathcal{SR}$ and other $\mu\mathcal{SR}$ techniques in some detail, but it is useful to begin with a qualitative phenomenological description just to establish some terminology. A crude apparatus for TF-$\mu^+\mathcal{SR}$ ($\mu\mathcal{SR}$ using positive muons) is pictured schematically in Fig. 1. The μ^+ arising from π^+ decay at rest is perfectly spin-polarized as it enters the sample; later, it decays asymmetrically with the decay positron emitted preferentially along the muon spin direction. After stopping $\sim 10^6$ muons in the target sample one obtains a time spectrum like that shown in Fig. 2 (top), which ideally has the following form:

$$N(t) = B + N_0\, e^{-t/\tau_\mu}\, [1 + A(t)] \quad (1)$$

where N_0 is an overall normalization, B is a time-independent background, $\tau_\mu = 2.197$ μs and $A(t)$ is the corresponding *asymmetry spectrum* shown in Fig. 2 (bottom), which can be extracted numerically from $N(t)$ as[1]

$$A(t) = \left[\frac{N(t) - B}{N_0}\right] e^{+t/\tau_\mu} - 1 \quad (2)$$

Except for an empirical multiplicative constant, $A(t)$ represents the

[1]In order to convert $N(t)$ to $A(t)$ one must know both B and N_0; fortunately, both constants can be extracted numerically from $N(t)$ in cases where the *period* of μ^+ Larmor precession is a negligible fraction of the muon lifetime. Treating $N(t)$ as a continuous function (the actual discrete sums can easily be deduced from the integrals below)

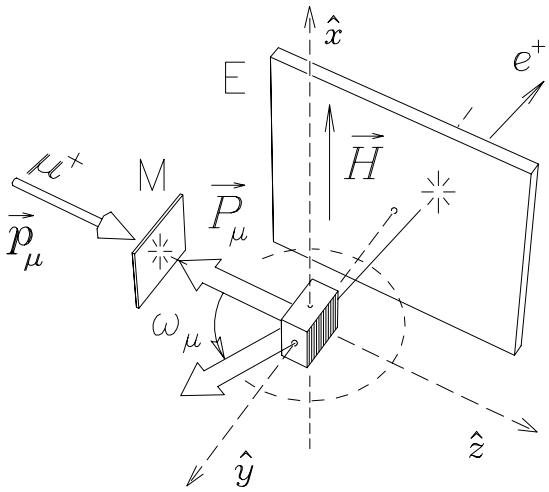

FIG. 1. A simple transverse-field (TF)-$\mu^+\mathcal{SR}$ experiment: the μ^+ beam enters from the left with its polarization antiparallel to its momentum. A magnetic field $\vec{\mathbf{H}}$ is applied vertically, causing the μ^+ spins to precess at the Larmor frequency $\omega_\mu = \gamma_\mu H$, where $\gamma_\mu/2\pi = 0.01355342$ MHz/Oe. An incoming μ^+ triggers the M counter, generating a *start* pulse for a fast time digitizer ("clock"), and an outgoing decay positron later stops the clock with a pulse from the E counter; for each such event the time interval is digitized and the corresponding bin in a discrete time spectrum is incremented.

time evolution of the muon polarization, much like a free induction decay (FID) signal in NMR.

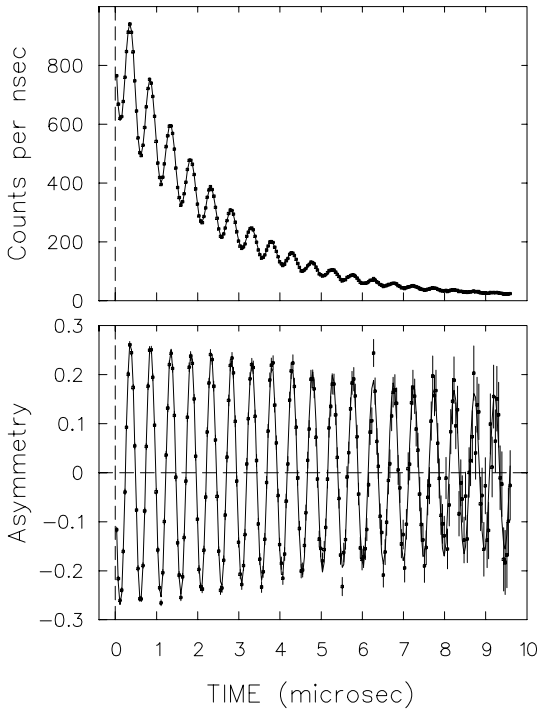

FIG. 2. TOP: "Raw" time spectrum from a simple TF-$\mu^+\mathcal{SR}$ experiment: the overall exponential decay reflects the muon lifetime and the precession of the μ^+ spins is manifest in the superimposed oscillations as the muon polarization sweeps past the positron detector.
BOTTOM: TF-$\mu^+\mathcal{SR}$ *asymmetry spectrum* obtained from the raw time spectrum by subtracting any time-independent background and dividing out the exponential distribution of muon decay times.

For the next decade or so after 1957, $\mu\mathcal{SR}$ was developed primarily in the guise of a series of experiments using muons to test the predictions of quantum electrodynamics ($\mathcal{QED}$) with unprecedented accuracy (Combley *et al.*, 1981; Hughes, 1988). Meanwhile the muon's weak-interaction properties were being precisely determined in an ongoing (Stoker *et al.*,

---

we may write

$$N_0 = \frac{S\tau_\mu E_+ - RT}{\tau_\mu^2 E_+ E_- - T^2} \qquad B = \frac{R\tau_\mu E_- - ST}{\tau_\mu^2 E_+ E_- - T^2}$$

where $S \equiv \int_{t_i}^{t_f} N(t)dt$, $R \equiv \int_{t_i}^{t_f} N(t)\exp(t/\tau_\mu)dt$, $E_\pm \equiv \pm[\exp(\pm t_f/\tau_\mu) - \exp(\pm t_i/\tau_\mu)]$ and $T \equiv t_f - t_i$, the time interval over which the integrals are evaluated.

1985) sequence of measurements of the *Michel parameters* (Michel, 1950) of normal muon decay. Many of today's areas of application of $\mu\mathcal{SR}$ began as peripheral problems in those fundamental physics experiments.

With the advent of the Meson Factories in the 1970's came a hundred- to thousand-fold increase in the intensity of muon beams, dramatically accelerating the development of new experimental techniques and the discovery of new applications for $\mu\mathcal{SR}$. When the potential of $\mu\mathcal{SR}$ became apparent, most Meson Factories invested in the upgrading of muon beamlines and $\mu\mathcal{SR}$ facilities that came on line in the early 1980's. Since then the techniques of $\mu\mathcal{SR}$ have been discovered by the chemistry and solid state physics communities and what was once an esoteric oddity has become one of the fastest growing areas of intermediate energy science.

Today's $\mu\mathcal{SR}$ is a standard magnetic resonance tool, almost exclusively devoted to disciplines rarely associated with subatomic physics — primarily chemistry and condensed matter physics. A list of some of these areas of application will appear later in this article, but first it is necessary to describe the fundamental physics that makes $\mu\mathcal{SR}$ possible and to explain the basic techniques of its use.

1. BASIC MUON PHYSICS

1.1 Muon Production

Although muons are produced in a variety of high-energy processes and elementary particle decays such as $K \to \mu + \nu$ decay (Yamazaki, 1984), $\mu\mathcal{SR}$ requires low energy muons in order to stop the beam in samples of convenient thickness ($\lesssim$ 1 cm) and these are available in the required intensities only from the ordinary two-body decay of charged pions:

$$\pi^+ \to \mu^+ + \nu_\mu \qquad \text{or} \qquad \pi^- \to \mu^- + \bar{\nu}_\mu \tag{3}$$

from which the muon emerges (in the rest frame of the pion) with a momentum of 29.79 MeV/c and a kinetic energy of 4.119 MeV. The lifetime of a free charged pion is τ_π =26.03 ns. Because the neutrino is only produced with negative helicity (spin antiparallel to momentum) and the antineutrino only with positive helicity — a succinct description of $\mathcal{P}$-nonconservation adequate for our purposes here — the simultaneous conservation of linear and angular momentum forces the μ^+ also to have negative helicity (and the μ^- positive helicity) in the rest frame of the pion. Thus muons emitted from pion decay at rest are also 100% spin polarized opposite to (for μ^+) or along (for μ^-) the direction of their momenta. This is the greatest advantage of $\mu\mathcal{SR}$ as a magnetic resonance technique: whereas NMR and ESR rely upon a thermal equilibrium spin polarization, usually achieved at low temperatures in strong magnetic fields, $\mu\mathcal{SR}$ begins with a *perfectly* polarized probe, regardless of conditions in the medium to be studied. It also implies that muon spin degrees of freedom usually start their evolution as far from thermal equilibrium as conceivable.

Most μ^+ beams today are literally emitted from π^+ decay at rest in the surface layer of the primary target where the pions themselves are produced by collisions of high energy

protons with target nuclei — hence the common mnemonic name, *surface muons* (Bowen, 1985). Unfortunately, this mode is not available for negative muons because a π^- stopping in the production target almost always undergoes nuclear capture from low-lying orbitals of pionic atoms before it has a chance to decay. This problem was actually solved long before the surface muon beam was invented, when many fundamental physics experiments with muons were primarily concerned with the "heavy electron" behaviour of the μ^-: in so-called "conventional" muon channels, pions are allowed to decay *in flight* down a relatively long straight section where the decay muons are collected by axial or alternating-gradient magnetic fields; the muons emitted "backward" in the pion rest frame have quite different momenta from those emitted forward (or from the pions themselves), and can thus be selectively extracted by a bending magnet. The disadvantages of such *backward muon beams* are their relatively higher momentum (usually $\sim$ 50-100 MeV/c), their larger momentum spread (and therefore lower stopping density) and their much larger phase space (and therefore lower luminosity). Today they are rarely used for $\mu^+\mathcal{SR}$, but for $\mu^-\mathcal{SR}$ there is no alternative.

1.2 Muon Decay

Books have been written on the subject of this section (Primakoff, 1975); there follows only a synopsis of those aspects of normal muon decay ($\mu^\pm \rightarrow e^\pm + \nu_{e,\mu} + \bar{\nu}_{\mu,e}$) that are essential to a qualitative understanding of $\mu\mathcal{SR}$. The foremost of these is, of course, the propensity of the muon decay positron [electron] to be emitted along [opposite to] the spin of the μ^+ [μ^-]. This second example of $\mathcal{P}$-nonconservation in the weak interaction is what allows us to read out the information encoded in the evolution of an initially polarized muon spin ensemble. The information is delivered to the experimenter in the form of rather high energy (up to 52 MeV) positrons or electrons, which readily penetrate sample holders, cryostats or ovens and the detectors used to establish the time and direction of the muon decay.

The decay probability of the muon, illustrated in Fig. 3, depends upon the $e^\pm$ energy $x \equiv \varepsilon_e/\varepsilon_{\max}$ (where $\varepsilon_{\max} = 52.83$ MeV is the maximum possible total relativistic energy of the $e^\pm$) and the angle θ between the muon spin direction and the direction of $e^\pm$ emission as

$$dP(x,\theta) = E(x)\,[1 + a(x)\cos\theta]\,dx\,d(\cos\theta) \tag{4}$$

The *asymmetry* factor a depends upon the $e^\pm$ energy as

$$a(x) = \pm\frac{2x-1}{3-2x} \tag{5}$$

and the normalized $e^\pm$ energy spectrum has the form

$$E(x) = 2x^2(3-2x). \tag{6}$$

Figure 4 shows the functions $E(x)/2$, $a(x)$ and their product. Note that a changes sign at low energy; however, very few positrons are emitted with such low energies (see above) and those which are will usually not be detected (see below).

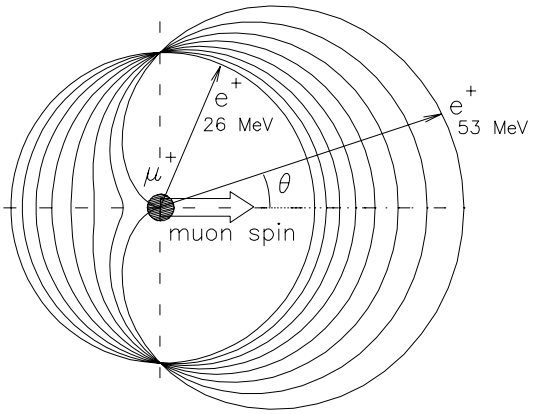

FIG. 3. Angular distribution of the e^+ from $\mu^+ \to e^+ + \nu_e + \bar{\nu}_\mu$ decay: the *asymmetry* (anisotropy) of the distribution is 100% for the highest $e^\pm$ energy $\varepsilon_{\max} = 52.83$ MeV and zero (*i.e.*, an isotropic distribution) for $\varepsilon_e = \varepsilon_{\max}/2$; for $\varepsilon_e \to 0$ (not shown) the asymmetry is negative.

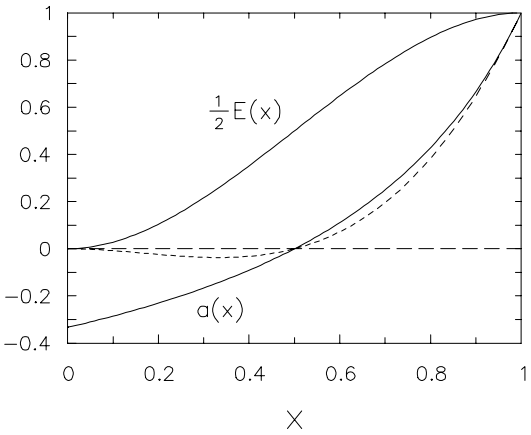

FIG. 4. Solid lines: energy spectrum $E(x)/2$ ($e^\pm$ energy $\varepsilon_e = x \cdot 52.83$ MeV) of $e^\pm$ from normal $\mu^\pm$ decay and ε_e-dependence of μ^+ decay asymmetry $a(x)$ [degree of correlation between e^+ momentum and μ^+ spin direction]. (For $\mu^- \to e^- \bar{\nu}_e \nu_\mu$, a has the opposite sign.) Dashed line: weighted $\mu^+ \to e^+ \nu_e \bar{\nu}_\mu$ asymmetry spectrum, the product of $E(x)/2$ and $a(x)$.

1.2.1 Asymmetry Calibration. The theoretical average asymmetry

$$\langle a \rangle \;=\; \int_0^1 a(x)E(x)dx \;=\; \pm\frac{1}{3} \qquad (7)$$

is never realized in practice (except by accident) for several reasons:

First, radiative corrections subtly distort the low-energy end of the spectrum (Sachs *et al.*, 1975).

Second, the low energy $e^\pm$ are easily stopped in even thin layers of material such as the wrappings of scintillation counters; indeed, since this effect raises the average asymmetry, it is common practice to insert degraders between the muon stopping region and the $e^\pm$ detectors, when feasible, up to an optimum range (*e.g.* $\approx$ 3-4 cm of graphite) that maximizes the product A^2N, where A is the empirical asymmetry (defined below) and N is the $e^\pm$ rate reaching the detector. (One should generally use low-Z materials for degraders in order to mimimize bremsstrahlung and pair production, which can greatly confuse the issue, unless one wishes to *use* such effects to bypass strong magnetic fields — see below.)

Third, a typical $e^\pm$ detector intercepts a rather large solid angle and thus averages $\cos\theta$ appreciably. The optimal detector geometry for general-purpose time-differential (TD)-$\mu\mathcal{SR}$ is a cube centered on the target where the muons stop, with each of the 6 faces a single detector. (Although in principle one could gain back some asymmetry by using position-sensitive detectors and weighting individual events according to the projections of the $e^\pm$ track along different axes, the

complications of counting statistics [not to mention the expense of processing such information at very high rates!] are not usually justified by the marginal improvement.)

Finally, because the decay $e^{\pm}$ will follow a helical path in an applied magnetic field $\vec{\mathbf{H}}$ (which is an essential part of many $\mu\mathcal{SR}$ experiments), the curling up of $e^{\pm}$ orbits causes the efficiency of their detection to be a function of both their energy and the applied field strength; the apparent direction of emission may also be affected. At $p_e = 30$ MeV/c (a typical $e^{\pm}$ momentum) the radius of curvature ρ_e of an orbit perpendicular to an applied magnetic field $H = 1$ T is exactly 10 cm, as given by the familiar formula

$$\rho[\mathrm{cm}] \;=\; \frac{p\ [\mathrm{MeV/c}]}{0.3\ H\ [\mathrm{kOe}]}. \qquad (8)$$

This effect becomes problematic at high fields ($H \gtrsim 5$ T $\Longrightarrow \rho \lesssim 2$ cm) in which case $\mu\mathcal{SR}$ requires very small samples and detectors. Another possible approach to this problem is to intentionally generate bremsstrahlung photons from the decay $e^{\pm}$ using a lead converter near the target and then reconvert the photons in front of the detector after they have traversed the high-field region.

Taken together, these systematic effects make the empirical asymmetry A in a given detector perplexingly dependent upon the thickness, geometry and material of target and detectors, not to mention magnetic field. Attempts to correct analytically for $e^{\pm}$ energy *etc.* are usually only reliable to within a few percent.

Fortunately there are many materials (including most metals) in which the μ^+ suffers negligible depolarization; thus the usual method for *calibrating the asymmetry* in $\mu^+\mathcal{SR}$ is to first measure a dummy sample of dimensions identical to those of the real sample, but made from aluminum or silver. If great care is taken to arrange the two samples in exactly the same position, this will determine the *empirical maximum asymmetry* A_0 to within a few percent of itself; typical values are 0.2 to 0.3. However, materials of the same nominal thickness (in g/cm^2) will often exhibit different dE/dx and multiple scattering of the $e^{\pm}$, so that this calibration method cannot generally be trusted to better than $\sim 1\%$.

In $\mu^-\mathcal{SR}$, as we shall see, such calibrations are much more difficult due to the loss of μ^- polarization in the initial cascade to the ground state of the muonic atom. To the author's knowledge there is no satisfactory solution for the A_0 calibration problem in $\mu^-\mathcal{SR}$. The usual method is to calibrate on graphite, which gives a residual μ^- polarization of about $17 \pm 2\%$ of the initial muon beam polarization (Kuno *et al.*, 1984).

1.3 The "Heavy Electron" *vs.* the "Light Proton"

Asymmetry calibration is perhaps the least of the qualitative differences between $\mu^+\mathcal{SR}$ and $\mu^-\mathcal{SR}$, all of which are consequences of the opposite charges of the μ^+ and μ^-. In elementary particle physics, the muon is often described as a "heavy electron" in reference to its family resemblance to other leptons; it is the μ^- that is so designated. Indeed, the μ^- does just what one might expect of a heavy electron: it under-

goes Coulomb capture into atomic orbitals analogous to those of electrons but 206.768 times closer to the nucleus and unrestricted by the Pauli exclusion principle; thus the muon quickly (usually in $\sim 10^{-14}$ s) cascades to the $1s$ ground state, emitting photons (known as muonic X-rays) and/or Auger electrons (ejected from low-lying orbitals in the same atom by muonic X-rays) on the way. Once there, the significant overlap between muon and nuclear wavefunctions [in heavy nuclei the muon spends most its time inside the mean nuclear radius] gives the weak interaction between the muon and the proton a chance to act, resulting in nuclear capture ($\mu^- + p \rightarrow n + \nu_\mu$) which appreciably reduces the μ^- lifetime (and the fraction of muons decaying to electrons for $\mu^-\mathcal{SR}$ to detect).

By contrast, the positive muon avoids positively charged nuclei and will capture its own electron when it can, to form the hydrogenlike atom muonium (μ^+e^-, usually abbreviated Mu). In fact, the qualitative behavior of the μ^+ in matter resembles that of a light proton far more than that of its closer antilepton relative, the positron. The μ^+ mass is 0.1126 times that of the proton but 206.768 times that of the positron; its magnetic moment is 3.1832 times that of the proton but only 0.48363% of the positron's. The Mu atom is almost identical (except in mass) to the hydrogen atom, whereas the positronium atom (e^+e^- or Ps) has no nucleus and half the binding energy of H. Positronium also annihilates very quickly, whereas weak electron capture in muonium ($\mu^+ + e^- \rightarrow \bar{\nu}_\mu + \nu_e$) only shortens the μ^+ lifetime by ~ 1 part in 10^{10}.

As a result, $\mu^-\mathcal{SR}$ differs qualitatively from $\mu^+\mathcal{SR}$:

Lifetime(s): The μ^+ lifetime is independent of its environment while that of the μ^- depends strongly upon the Z of the nucleus it becomes attached to; a sample containing several elements will have as many μ^- lifetimes, the ratios of whose probabilities cannot be reliably estimated from the Fermi-Teller "Z law" (Fermi and Teller, 1947) and therefore must be determined by fitting the time distribution of decay or capture products.

Muon Capture: A μ^- that undergoes nuclear capture ($\mu^- + p \rightarrow n + \nu_\mu$) does not produce a decay electron for detection in $\mu^-\mathcal{SR}$; the $\mu^-\mathcal{SR}$ event rate per incident muon is thus proportional to the μ^- lifetime, which in high-Z elements can be as little as 4% of the free muon lifetime. This rate loss can often be offset by increasing the μ^- beam intensity, except when the sample contains both heavy and light nuclei.

Heterogeneous Signal: Whereas the μ^+ produces only positrons and undetected neutrinos, a μ^- entering some high-Z samples like ^{238}U is likely to cause emission of X-rays and Auger electrons during the atomic cascade, fission fragments and neutrons (on average several per muon) from either nuclear muon capture or nuclear internal conversion of muonic X-rays, as well as the occasional decay electron. The $\mu^-\mathcal{SR}$ signal is therefore noisy and heterogeneous. This does make it rather interesting from the points of view of atomic and nuclear physics, but such complications are so far unwelcome in historically typical $\mu^-\mathcal{SR}$

applications.

Lost Polarization: Spin-orbit coupling in the atomic cascade leaves the μ^- in its ground state $1s$ orbital with a dramatically reduced spin polarization, typically $\lesssim 20\%$. Because statistical uncertainties shrink as $N^{-1/2}$ one must accumulate 25 times more events to achieve the same statistical accuracy in measuring a 5 times smaller signal. This seemingly irreducible disadvantage is the main limitation of $\mu^-\mathcal{SR}$ applications and is the reason why $\mu\mathcal{SR}$ is often treated as synonymous with $\mu^+\mathcal{SR}$. However, since $\mu^-\mathcal{SR}$ offers complementary and unique information, it will always be an essential part of the $\mu\mathcal{SR}$ repertoire. There is also a chance that new techniques such as X-ray tagged $\mu^-\mathcal{SR}$ may help overcome this disadvantage.

Hyperfine Effects: The hyperfine coupling between the muon and nuclear spins in nonzero-spin nuclei is enormous, often large enough to cause Auger emission of K and L electrons (Winston, 1963). The two hyperfine states F^+ and F^- of the $1s$ muonic atom (in which the muon spin is respectively parallel and antiparallel to the nuclear spin) therefore produce distinct $\mu^-\mathcal{SR}$ signals, each with its own characteristic precession frequency, in such systems. This was long thought to limit useful $\mu^-\mathcal{SR}$ to spinless elements, but quite a few nuclei with spin $I > 1/2$ have been found to exhibit potentially useful $\mu^-\mathcal{SR}$ signals, albeit at reduced amplitudes (Brewer, 1984a/b).

Taking into account the different lifetimes, cascade depolarizations and spin states of negative muons in different muonic atoms, we may generalize Eq. (1) to obtain the most general form for *electron-triggered* $\mu^-\mathcal{SR}$ in a sample composed of different elements:

$$N(t) \;=\; B \;+\; \sum_i N_i^0\, e^{-t/\tau_i}\; [1 + A_i(t)] \tag{9}$$

in which $N_i^0 = N_0 f_i(\tau_i/\tau_\mu)$, where N_0 is an overall normalization, f_i is the fraction of muons captured on the i^{th} type of nucleus and τ_i is the μ^- lifetime in that species of muonic atom and hyperfine state; $A_i(t) = A_0 P_i(t)$, where A_0 is a common maximal asymmetry factor and $P_i(t)$ is the polarization of muons in the i^{th} type of muonic atoms. For TF-$\mu^-\mathcal{SR}$, this polarization will have the form $P_i(t) = P_i^0 G_i(t)\cos(\omega_i t + \phi_i)$, where P_i^0 is the polarization remaining in that atom's given hyperfine state after the cascade, $G_i(t)$ is the corresponding relaxation function (see below), ω_i is its characteristic precession frequency in the applied magnetic field and ϕ_i is the initial phase.

In the interest of simplicity, further discussion of $\mu^-\mathcal{SR}$ will be neglected in favour of $\mu^+\mathcal{SR}$, which occupies most of the attention of the $\mu\mathcal{SR}$ community.

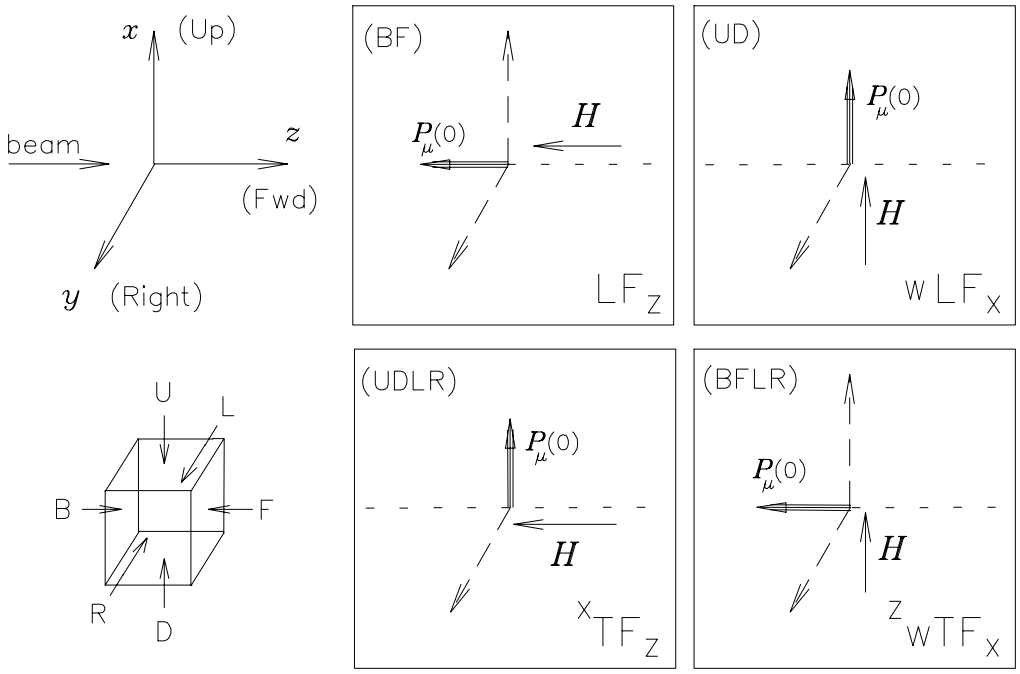

FIG. 5. Coordinate system and labelling conventions for surface muon $\mu\mathcal{SR}$ experiments. Note that the superscript on the left indicates the direction of the incoming muon polarization while the subscript on the right indicates the direction of the applied field (if any); for longitudinal field (LF) and by continuation for zero field (ZF) both will always be the same, but for TF there are in principle two possible arrangements for each choice of super(sub)script. (For instance, ${}^{z}w\mathrm{TF}_{y}$ *vs.* ${}^{x}w\mathrm{TF}_{y}$.) "Weak" (w) field means "not strong enough to deflect the muon beam appreciably."

2. $\mu\mathcal{SR}$ TECHNIQUES

Ideally (and often in reality) the $\mu\mathcal{SR}$ experimenter has control over the orientation of the detectors, the applied magnetic field and (within some range) the muons' spin polarization. The beam momentum can be deflected as well, but this is rarely desirable. In order to consistently designate different orientation choices, the labelling conventions defined in Fig. 5 have been devised specifically for $\mu^{+}\mathcal{SR}$ experiments using surface muons, which are originally polarized opposite to their momentum but whose spins can be rotated 90° by a Wien filter in the beamline (Brewer, 1981). [Such flexibility is not available for conventional or "backward" $\mu^{\pm}$ beams, which will be neglected here partly for that reason.] The standard detector array consists of six counters aligned with the positive and negative coordinate axes and labelled F (forward), B (backward), U (up), D (down), L (left) and R (right) according to a "beam's-eye view" naming convention. Note that the unrotated muon polarization points toward the B counter and in the spin-rotated mode toward the U counter; the latter depends, of course, on the orientation of the fields in the Wien filter.

2.1 Time-Differential $\mu\mathcal{SR}$ in Transverse Field

The simplest and most familiar time-differential (TD)-$\mu\mathcal{SR}$ technique is the transverse field (TF) muon spin *rotation* experiment, in which an external magnetic field is applied perpendicular (transverse) to the muon polarization, causing the muon spins to *precess* (rotate) about the field.

2.1.1 The Basic Technique. In transverse-field (TF)-$\mu\mathcal{SR}$ a magnetic field $\vec{\mathbf{H}}$ is applied perpendicular to the initial muon spin direction, causing Larmor precession of the muon polarization about $\vec{\mathbf{H}}$. This arrangement varies from the primitive version depicted in Fig. 1 to the 4-counter, spin-rotated ${}^{x}\mathrm{TF}_{z}$-$\mu\mathcal{SR}$ apparatus shown in Fig. 6 and the ${}^{z}\mathrm{TF}_{x}$-$\mu\mathcal{SR}$ arrangement in Fig. 7, each of which illustrates *quadrature* detection (two orthogonal pairs of opposing counters in the plane perpendicular to the applied field); but the time spectra from individual counters all have the qualitative appearance shown in Fig. 2.

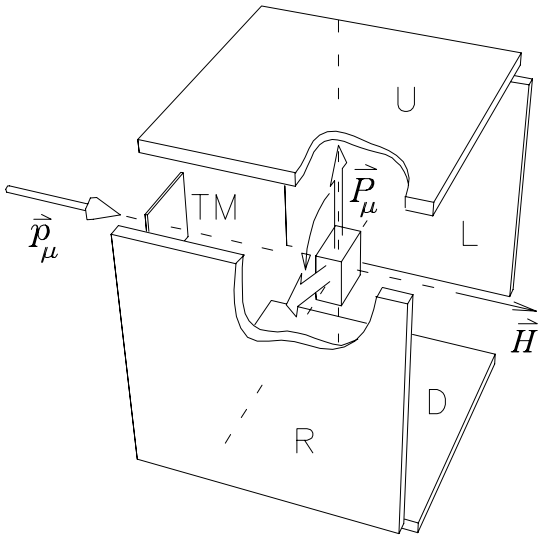

FIG. 6. Counter arrangements for ${}^{x}\mathrm{TF}_{z}$-$\mu\mathcal{SR}$, in which the muon beam has been passed through a Wien filter to rotate the muon spins until they are perpendicular to their momenta. The momentum $\vec{\mathbf{p}}_\mu$ is undeflected in the magnetic field $\vec{\mathbf{H}} = H\hat{z} \parallel \vec{\mathbf{p}}_\mu$ but the polarization $\vec{\mathbf{P}}_\mu$ precesses in the x-y plane.

Frequency: The most obvious observable in a TF-$\mu\mathcal{SR}$ spectrum is the *muon precession frequency* $\omega_\mu = \gamma_\mu B$, which (thanks to our precise knowledge of γ_μ) is equivalent to the local magnetic field B at the muon. Since B may be affected by diamagnetism, paramagnetism and contact hyperfine interactions with polarized electrons (Knight shifts) in the medium, B is generally different from the applied field H_0; this difference is often the main focus of the TF-$\mu\mathcal{SR}$ experiment. An example is shown in Fig. 8.

Asymmetry: The second obvious parameter characterizing muon precession in a transverse field is the amplitude or *asymmetry* of the precession signal. As mentioned earlier, the absolute calibration of this amplitude is tricky but one can usually convert the initial amplitude into a *residual polarization* with an accuracy of a few percent. In metallic samples the initial polarization is generally consistent with 100%, but in insulators or semiconductors, liquids or gases, some fraction of the muons (ranging from 0 to 100%) either form muonium (Mu) or experience some other form of depolarization in the early ($\lesssim 1$ ns) stages of thermalization in the sample.

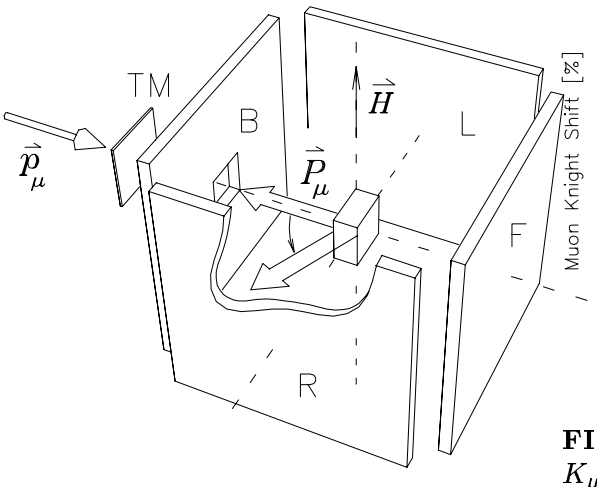

FIG. 7. Counter arrangements for ${}^{z}w\mathrm{TF}_{x}$-$\mu^+\mathcal{SR}$, in which the μ^+ beam still has its polarization antiparallel to its momentum. The field must therefore be perpendicular to both $\vec{\mathbf{p}}_\mu$ and $\vec{\mathbf{P}}_\mu$ which restricts use with surface muon beams to weak fields $H \lesssim 100$ Oe.

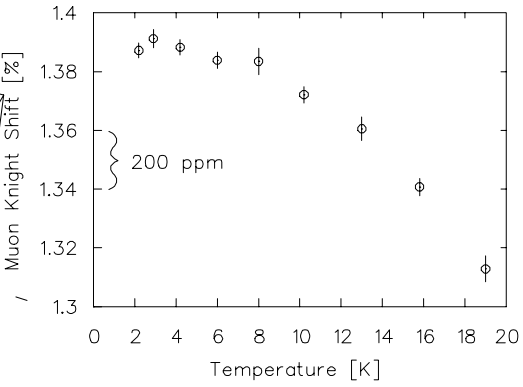

FIG. 8. Positive muon Knight shift $K_\mu \equiv (B_\mu - H_0)/H_0$ (where H_0 is the applied magnetic field and B_μ is the field at the muon) as a function of temperature in a single crystal of antimony with the $\hat{c}$ axis parallel to the applied field (1.5 T). The precision (approximately ± 50 ppm) is typical of what can easily be achieved with routine methods in modest TF-$\mu\mathcal{SR}$ experiments; much higher precision is possible with refined techniques (see the later section on *strobo-*$\mu\mathcal{SR}$).

The effect of Mu formation in wTF is to cause the muon polarization to precess in the opposite sense to that of muons in diamagnetic environments, roughly 103 times faster; this results in dramatic "dephasing" if the Mu atoms subsequently react at exponentially distributed times to enter diamagnetic states. If all this takes place within a few ns, all one can observe is the net effect on the subsequent diamagnetic μ^+ precession signal, namely a reduction of asymmetry and a simultaneous shift of the apparent initial phase of precession. If the magnetic field is in the $\hat{z}$ direction and the initial μ^+ polarization is in the $\hat{x}$ direction, we may define the *complex* muon polarization $\tilde{P}(t) \equiv P_x(t) + iP_y(t)$, in terms of which the overall polarization of an ensemble of muons starting as Mu atoms and reacting at a rate Λ to form some diamagnetic species is given in the low-field limit (averaging over high-frequency hyperfine oscillations) by

$$\tilde{P}(t) \approx \frac{1}{2}\,\frac{\omega_{\mathrm{Mu}}+\omega_\mu}{\omega_{\mathrm{Mu}}+\omega_\mu - i\Lambda}\,e^{-(\Lambda+i\omega_{\mathrm{Mu}})t} + \frac{1}{2}\left[\frac{i\Lambda}{i\Lambda-(\omega_{\mathrm{Mu}}+\omega_\mu)} + \frac{\Lambda^2}{\Lambda^2+\omega_0^2}\right] \quad (10)$$

where the diamagnetic precession frequency is ω_μ and the muonium precession frequency is $\omega_{\mathrm{Mu}} \approx 103\omega_\mu$ in the opposite sense. This sort of simple *residual polarization* picture also describes many other *delayed formation* scenarios.

Initial Phase of precession: A more subtle aspect of the residual polarization picture is the shift of the appar-

ent initial phase of the μ^+ precession due to (*e.g.*) the formation of short-lived Mu atoms precessing in the opposite sense. Measurement of such *phase shifts* has often proved valuable in sorting out "fast chemistry" effects (Brewer *et al.*, 1974).

"Relaxation:" Following thermalization of translational degrees of freedom, which may take as little as 100 ps in solids, the muon precession signal may still decrease in amplitude due to "dephasing" (T_2 effects) or true irreversible relaxation processes (T_1 effects). The latter are more often studied in longitudinal field (LF) where the distinction between T_1 and T_2 is not subject to so much semantic debate. (See later section on "relaxation" in LF-$\mu\mathcal{SR}$.) Depolarization due to inhomogeneous magnetic fields often takes the form of a gaussian relaxation function $\exp(-\frac{1}{2}\sigma^2 t^2)$ as shown in Fig. 9.

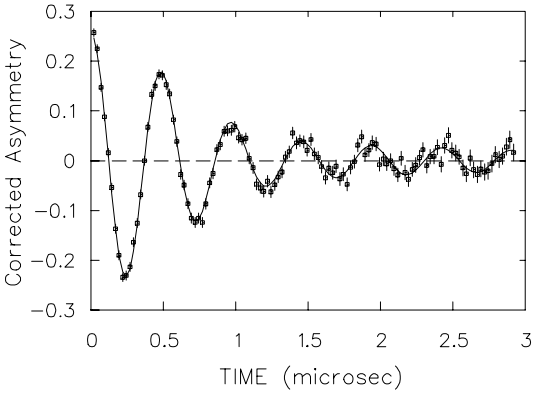

FIG. 9. Depolarization of muons in a sintered powder of superconducting $La_{1.85}\mathcal{SR}_{0.15}CuO_4$ at 10 K in an applied magnetic field of 150 Oe. The relaxation is due to local field inhomogeneities caused by flux exclusion and a *vortex lattice* in this type II superconductor; it is adequately described by a gaussian relaxation function in which $\sigma \propto \lambda^{-2}$ where λ is the London penetration depth. This has been much used for initial estimates of λ.

Muonium Precession: All the features just described for muon precession at the diamagnetic Larmor frequency $\omega_\mu = \gamma_\mu H$ are also often seen for *muonium precession* in wTF-$\mu\mathcal{SR}$ experiments. The main differences are that $\omega_{\rm Mu} = \gamma_{\rm Mu} H$ is roughly 103 times larger than ω_μ in the same field H [due to the huge magnetic moment of the electron locked to the muon spin by the hyperfine interaction], that the sense of wTF Mu precession is opposite to that of the free μ^+ [due to the opposite sign of the dominating e^- moment], that half the muon polarization appears lost in most experiments [due to the fast (4463 MHz for Mu in vacuum) hyperfine oscillations between the $|\Uparrow\downarrow\rangle$ and $|\Downarrow\uparrow\rangle$ states, where $\Updownarrow$ refers to the electron spin and $\updownarrow$ refers to that of the muon] and that $\omega_{\rm Mu}$ *splits* into two frequencies for $H \gtrsim 20$ Oe because the hyperfine interaction is finite. This phenomenon will be discussed in more detail below.

2.1.2 High Field. Since the period of muon precession is 7.38 ns in a field of 1 T and is inversely proportional to H, it is not difficult to achieve a magnetic field strong enough to challenge the time resolution of most $\mu\mathcal{SR}$ spectrometers. Moreover, the radius of decay positron orbits shrinks with increasing field until experiments in $H \gtrsim 5$ T require small detectors within 1-2 cm of the sample. Nevertheless, the effort of miniaturization and state-of-the-art

time resolution is often justified by the improved resolution for Knight shifts and/or access to intrinsically high-field phenomena. In high fields a standard TD-$\mu\mathcal{SR}$ time spectrum consists of a large number of small time bins, each of which may have a rather low number of counts and a correspondingly large statistical uncertainty; this circumstance makes the usual lab frame asymmetry plot rather uninformative to the eye and expensive to fit by χ^2 minimization, motivating new methods of data analysis.

Fourier Transforms: Often, especially when high frequencies are involved, one would rather see a frequency spectrum than a time spectrum. The art of converting the latter into the former is subject to continuing evolution and perpetual debate, but virtually all $\mu\mathcal{SR}$ facilities include the fast fourier transform (FFT) in their standard data analysis tools. A complete account of the merits and hazards of such treatments is beyond the scope of this article, but it is useful to point out several ubiquitous features that are ignored at one's peril.

First, as show in Fig. 10, the fact that the time range of a $\mu\mathcal{SR}$ spectrum necessarily starts at $t = 0$ means that the imaginary (odd in t) part of the resultant frequency spectrum is dramatically broadened by the tacit presence of the Heaviside function; this has nothing to do with either the muon lifetime or the finite range of positive time. Thus the real part of the amplitude (the proper objective of our FFT) may be quite narrow but the square root of the power spectrum (the sum of the squares of the real and imaginary parts) will still be very broad. Various tricks are available for unmixing the real and imaginary parts.

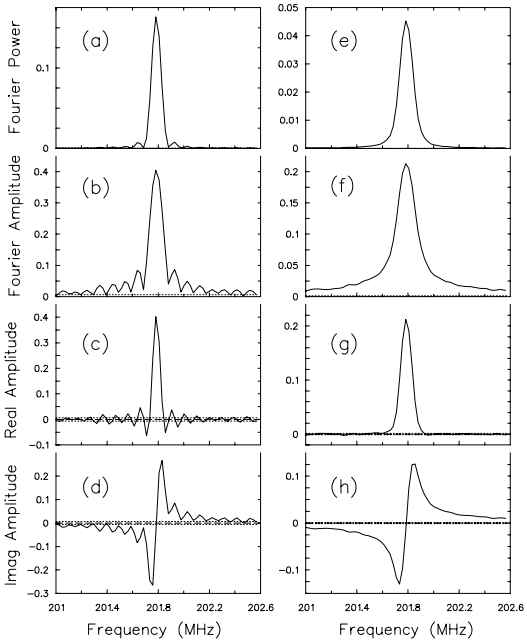

FIG. 10. Results of complex FFT of a *quadrature* $\mu^+\mathcal{SR}$ time spectrum with a slow relaxation rate: (a) through (d) show the power, the amplitude (square root of the power), the real and the imaginary parts of the frequency spectrum resulting from FFT of the "raw" complex time spectum over 10.24 μs at a field of 1.489 T; (e) through (h) show the same quantities for the same data *apodized* by a gaussian envelope function with a 4 μs time constant.

Second, because of the finite muon lifetime there are less statistics in the bins at late times and consequently the "error bars" in the asymmetry spectrum grow exponentially with time as $\exp(+t/2\tau_\mu)$. (See Fig. 2.) This introduces noise in an annoyingly non-uniform way, which may in principle be corrected for using not-so-fast fourier transform methods. These *noise effects* are always

subject to suppression *without limit* (except for the finite patience of the experimenter) by simply taking more statistics; although the finite muon lifetime is responsible, it does *not* fix any absolute limits on precision — only practical ones.

Third, because experimenters' patience is indeed finite, most $\mu\mathcal{SR}$ time spectra only extend to 10-20 μs; thus the FFT is cut off abruptly at some time limit, introducing the "ringing" effect evident on the left side of Fig. 10. This can be suppressed by *apodization* — multiplying the "raw" time spectrum by an *envelope function* that causes the product to go to zero gently before the abrupt end of the time range. As evident from Fig. 10, well-chosen apodization removes the ringing caused by FFT on a finite time interval but introduces a line-broadening effect that must be taken into account in the interpretation.

In general, there are no time space $\leftrightarrow$ frequency space interconversions or interpretations that make everyone happy; hence the earlier reference to such devices as "art." However, like other art forms the FFT can produce some very pleasing results; for example, Fig. 11 shows the frequency (and thus internal magnetic field) spectrum from $\mu^+\mathcal{SR}$ in superconducting $YBa_2Cu_3O_{6.95}$.

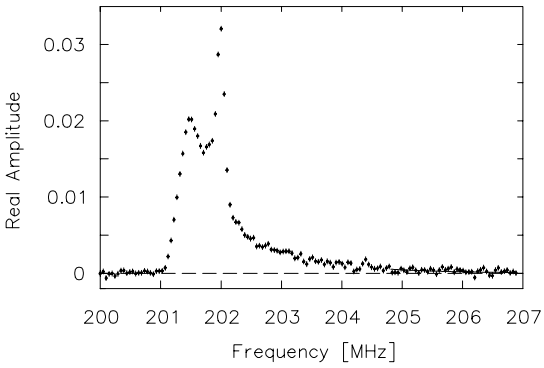

FIG. 11. Real part of frequency spectrum taken at a temperature of 6 K for positive muons in a *single* (3 mm × 3 mm × 0.2 mm) crystal of superconducting $YBa_2Cu_3O_{6.95}$ (a type II superconductor with T_c = 92 K) cooled in a field of 1.489 T applied along the crystalline $\hat{c}$ axis. The sharp peak at 202 MHz is due to muons missing the superconductor and stopping in a normal region where the field distribution is not broadened by the vortex lattice.

Rotating Reference Frames: For TF-$\mu\mathcal{SR}$ in high magnetic field (HTF-$\mu\mathcal{SR}$), another essential tool is the *rotating reference frame* (RRF) transformation, an example of which is shown in Fig. 12. The following description will omit the details of transforming discrete spectra and give only a simplified treatment in terms of an idealized continuous time spectrum. In fact, the RRF transformation works best on *orthogonal pairs* of spectra — as for instance when the magnetic field acts in the $\hat{z}$ direction and detectors are situated in the $\pm\hat{x}$ and $\pm\hat{y}$ directions defining the plane of precession of the muon polarization — where a *complex* asymmetry spectrum $\tilde{A}(t)$ can be defined as (*e.g.*) $\tilde{A}(t) \equiv A_x(t) + iA_y(t)$. In this case the RRF transformation is simply

$$\tilde{A}_{\rm RRF}(t) \;=\; \tilde{A}(t)\, e^{-i\Omega t} \qquad (11)$$

where Ω is the RRF frequency — chosen arbitrarily to produce a transformed $\tilde{A}_{\rm RRF}(t)$ with the desired characteristics. For instance, if the muons precess at a high frequency ω_μ, one may select Ω slightly smaller than ω_μ

to produce a $\tilde{A}_{\mathrm{RRF}}(t)$ which varies relatively slowly with time; the resulting complex spectrum can be *packed* (n_p original time bins $\rightarrow$ one coarser time bin) in which case the statistical uncertainties of individual bins are reduced by a factor roughly equal to $\sqrt{n_p}$.

FIG. 12. The first 4.5 μs of a $\mu^+\mathcal{SR}$ time spectrum taken at roughly 0.2 T in the lab frame where the data are recorded and in the rotating reference frame (RRF) to which it has been transformed numerically for display and fitting. The RRF frequency of 21.2 MHz is chosen to produce a slow precession signal for visual clarity. Because the original spectrum is real (no orthogonal detector arrays) the maximum amplitude in each of the complex RRF spectra (real part: circles; imaginary part: triangles) is actually a factor of two smaller than in the lab frame. The solid line in the RRF spectra is a fit to three frequencies; a single frequency (or even two) would result in a much poorer fit to the data.

There are several advantages to such a transformation: first and most obvious is the reduction (by a factor of n_p) of the number of bins to be fitted in analysis programs, a straightforward improvement of efficiency; second and probably more important is the transformation of a large number of narrow time bins (with statistical uncertainties often larger than the signals under scrutiny) into a small number of well-defined bins representing the signal in a form that allows convenient display and visual inspection.

In the event that a single spectrum contains several signals at drastically different frequencies ω_i, separate RRF transformations at frequencies $\Omega_i \approx \omega_i$ can be used to isolate each signal for easy fitting.

It is also possible to perform a RRF transformation on a pure real spectrum (*i.e.*, one without orthogonal detector axes) if care is taken to select Ω and n_p so as to "bin out" the spurious signal at the RRF frequency (Riseman and Brewer, 1990).

2.1.3 Paramagnetic States. The use of fourier transforms to reveal *lineshapes* is actually a recent application in $\mu\mathcal{SR}$; the oldest and still most widespread use of FFT in $\mu\mathcal{SR}$ is for extracting the frequency spectrum of muons in *paramagnetic* states such as muonium or radicals (molecules containing one or more unpaired electrons) in which the muon spin is strongly coupled to electron spins (or, in principle, orbital moments) by *hyperfine* interactions. The behaviour of the simplest case, two spin-1/2 particles coupled by a scalar contact

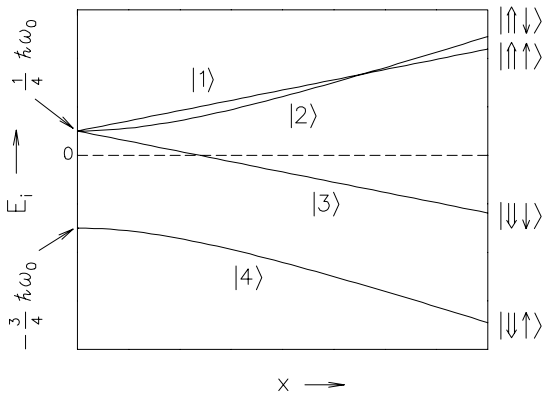

FIG. 13. *Breit-Rabi diagram* showing the energy levels of a system of two spin-1/2 particles of opposite sign and different magnetic moments — *e.g.*, muonium — as functions of the *reduced field* $x \equiv H/H_0$ where H_0 (1585 Oe for Mu in vacuum) is a characteristic *hyperfine field*. For the purpose of illustration, unphysical values of moments and coupling constants have been used. The *hyperfine frequency* $\nu_0 \equiv \omega_0/2\pi$ has the value 4463 MHz for muonium in vacuum. In zero field the three *triplet* ($J = 1$) eigenstates $|1\rangle$, $|2\rangle$ and $|3\rangle$ are degenerate and the *singlet* ($J = 0$) ground state $|4\rangle$ is $\hbar\omega_0$ lower in energy. At high reduced field ($x \to \infty$) the eigenstates are $|1\rangle \to |\Uparrow\uparrow\rangle$, $|2\rangle \to |\Uparrow\downarrow\rangle$, $|3\rangle \to |\Downarrow\downarrow\rangle$ and $|4\rangle \to |\Downarrow\uparrow\rangle$. ($\Updownarrow$ refers to the electron spin and $\updownarrow$ refers to that of the muon.) Note that state $|1\rangle$ is *lower* energy than state $|2\rangle$ above $H_c = \omega_0(\gamma_e - \gamma_\mu)/(2\gamma_e\gamma_\mu)$ [16.386 T for Mu in vacuum].

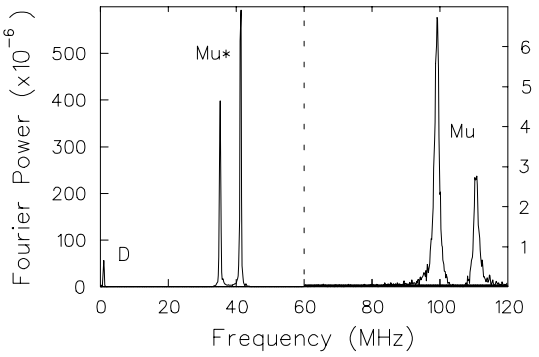

FIG. 14. Frequency power spectrum of positive muons in a pure silicon crystal at 10 K and 75 Oe transverse field showing the diamagnetic (D) signal, the rapidly-diffusing muonium (Mu) signals and the signals from so-called "anomalous" muonium (Mu*) which has been shown to be a muonium atom localized on a Si-Si bond center. Note vertical scale change at 60 MHz. After (Brewer *et al.*, 1973).

interaction in an applied magnetic field, is pictured in Fig. 13. Such couplings cause the μ^+e^- spin system (for example) to respond as a whole to applied magnetic fields, often producing rich and informative structure in the frequency spectrum (Patterson, 1988). A classic example is shown in Fig. 14 and a more recent case in Fig. 15.

2.2 Time-Differential $\mu\mathcal{SR}$ in Longitudinal and Zero Field

Referring again to Fig. 5, consider now the time evolution of the muon polarization in a magnetic field paralled to its initial direction (longitudinal field or LF). If the muon polarization initially has no components perpendicular to the local field then none will develop and only the polarization along the initial direction needs to be measured. Figure 16 illustrates the most common configuration and Fig. 17 shows an alternate scheme sometimes used with spin-rotated beams.

2.2.1 Two-Counter Asymmetry. The perceptive reader will have noticed several figures with vertical axes labelled, "Corrected Asymmetry." This is in reference to the fact that $\mu\mathcal{SR}$ time spectra taken in a

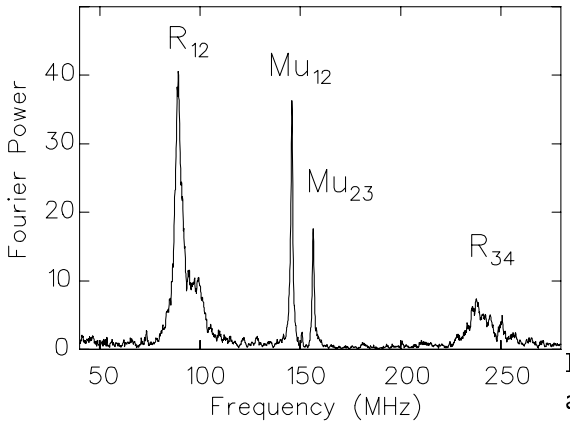

FIG. 15. Frequency power spectrum for positive muons in powdered buckminsterfullerite (crystalline C_{60}) at room temperature and 108 Oe (Kiefl *et al.*, 1992b), showing simultaneously the signals from muons in the $C_{60}Mu\cdot$ radical (R_{12} and R_{34}) and the endohedral muonium ($Mu@C_{60}$) atom (Mu_{12} and Mu_{23}). In paramagnetic molecules with nuclear moments, such radical signals cannot be seen in low field due to nuclear hyperfine broadening.

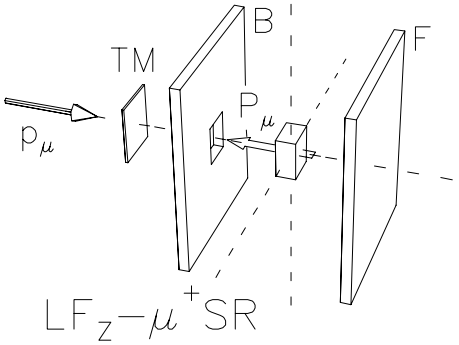

FIG. 16. Longitudinal-field $\mu\mathcal{SR}$ counter arrangement for LF_z-$\mu^+\mathcal{SR}$, in which the μ^+ beam is polarized antiparallel to its momentum. As $\vec{\mathbf{H}} = H\hat{z} \parallel \vec{\mathbf{p}}_\mu \parallel \vec{\mathbf{P}}_\mu$ any magnetic field strength may be utilized.

longitudinal geometry cannot be converted to asymmetry spectra using Eq. (2) because neither N_0 nor B can be extracted numerically from the data without some model of the time dependence of the longitudinal polarization. Instead one combines the time spectra from two detectors on opposite sides of the sample, such as "U" and "D" in Fig. 17, in the following way. First define the parameters

$\epsilon_{\rm U,D}$ = efficiency of U or D e detector

$B_{\rm U,D}$ = backgound in said e detector (measured using "$t < 0$ bins")

$A_{\rm U,D}$ = intrinsic asymmetry of e detector [Count rate $\sim (1 \pm A_{\rm U,D})$ for muons fully polarized along (opposite) detector symmetry axis.]

$P_x(t)$ = muon polarization along axis.

Thus

$$N_{\rm U,D}(t) = B_{\rm U,D} + N_0\epsilon_{\rm U,D}[1 \pm A_{\rm U,D}P_x(t)]$$

where N_0 is a common normalization.

The Experimental Asymmetry $a(t)$ is then obtained from either

$$a(t) \equiv \frac{[N_U(t) - B_U] - [N_D(t) - B_D]}{[N_U(t) - B_U] + [N_D(t) - B_D]} \quad \text{or}$$

$$a(t) = \frac{(1-\alpha) + (1+\alpha\beta)A_U P_x(t)}{(1+\alpha) + (1-\alpha\beta)A_U P_x(t)} \qquad (12)$$

$$\text{where} \quad \alpha \equiv \frac{\epsilon_D}{\epsilon_U} \quad \text{and} \quad \beta \equiv \frac{A_D}{A_U}. \qquad (13)$$

Thus $(1-\alpha)/(1+\alpha)$ is the "baseline" asymmetry for totally unpolarized muons.

The "Corrected" Asymmetry: In addition to the obvious "baseline shift" there is also a more subtle distortion in $a(t)$ for $\alpha\beta \neq 1$: a plot of $a(t)$ looks as if it has a nonlinear scale for the

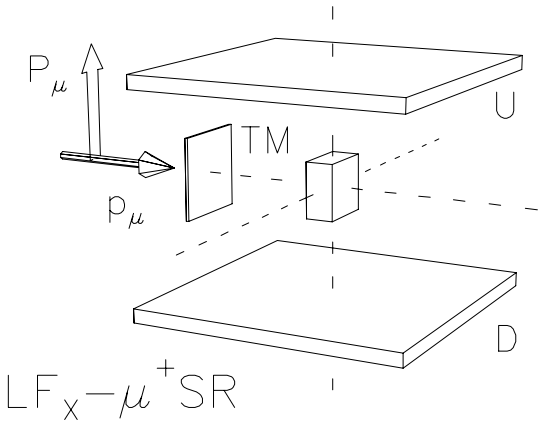

FIG. 17. Longitudinal-field $\mu\mathcal{SR}$ counter arrangement for LF$_x$-$\mu\mathcal{SR}$, in which the muon beam arrives spin-rotated by a Wien filter. Since the field is now perpendicular to $\vec{\mathbf{p}}_\mu$, use with surface muon beams is restricted to weak fields $H \lesssim 100$ Oe.

abcissa. To completely remove these distortions one must somehow independently determine α and β (usually by fitting data taken in wTF with the same geometry) and then apply the correction

$$A_U P_x(t) = \frac{(\alpha-1)+(\alpha+1)a(t)}{(\alpha\beta+1)+(\alpha\beta-1)a(t)}. \qquad (14)$$

These corrections apply equally to TF-$\mu\mathcal{SR}$ asymmetry spectra formed from opposing pairs of detectors; in fact these are usually used to fit for α. However, β must be determined from simultaneous fits to the opposing "raw" spectra $N_{\mathrm{U,D}}(t)$ in TF. It is not unusual to assume $\beta = 1$, although in principle one should always determine this empirical parameter as accurately as possible.

2.2.2 Zero Field. By extension, the field may be zero (ZF-$\mu\mathcal{SR}$) in which case all the same arguments hold as for LF-$\mu\mathcal{SR}$ and one measures the time evolution of the muon polarization along its original direction. In $\mu\mathcal{SR}$ this is just a routine extension of LF, but it bears emphasis since ZF is not so simple (though not impossible) in other magnetic resonance techniques.

2.2.3 "Relaxation." One consequence of the ease with which one can reduce the field to zero in a LF-$\mu\mathcal{SR}$ experiment is that conventional notions of *longitudinal* (T_1) *vs transverse* (T_2) relaxation processes often become confused and subject to bitter semantic arguments. In NMR, longitudinal relaxation generally occurs in a strong LF so that a change of polarization requires unambiguous transitions between Zeeman energy eigenstates of the probe spin. It is then easy to define the longitudinal relaxation rate T_1^{-1} in terms of such spin-lattice relaxation processes. Moreover, in strong transverse fields where the Zeeman energies are much greater than any local couplings (such as dipole-dipole interactions between the probe spin and nearby magnetic moments) it is easy to define a transverse relaxation rate T_2^{-1} in terms of the *dephasing* of probe spins precessing at slightly different frequencies due to small differences in the local field strength at different sites.

As noted by (Kubo and Toyabe, 1966), these distinctions are blurred and the terminology becomes less useful as the applied field becomes comparable to the local fields and eventually goes to zero. Basically, if the components of local fields transverse to the applied field are non-negligible in the vector sum forming the total field at the probe, then even in

this classical picture the relaxation phenomena become quite complicated and are still being worked out today (Dalmas-de-Reotier *et al.*, 1992). A broad review of this subject is impossible here, but a few examples can help to illustrate the potential of ZF- and LF-$\mu\mathcal{SR}$.

Nuclear Dipolar Relaxation: In the presence of strong electric field gradients, nuclei with electric quadrupole moments (such as Cu) exert an effective classical dipolar field on the muon:

$$\vec{\mathbf{B}}_{\rm dip} = \hbar\gamma_n J_q[3(\hat{r}\cdot\hat{q})\hat{r} - \hat{q}]/r^3 \qquad (15)$$

where γ_n is the nuclear gyromagnetic ratio, J_q is the component of nuclear spin along the electric field gradient direction $\hat{q}$ and $\hat{r} = \vec{\mathbf{r}}/r$ where $\vec{\mathbf{r}}$ is the vector of length r from the muon to the nucleus. The muon usually has several near neighbor nuclei generating a broad and nearly isotropic distribution of nuclear dipolar fields. Assuming a gaussian distribution of internal fields with random orientation leads to a muon polarization function (Hayano *et al.*, 1979)

$$g_{zz}^{\rm KT}(t) = \frac{1}{3} + \frac{2}{3}\left(1 - \Delta^2 t^2\right) e^{-\frac{1}{2}\Delta^2 t^2} \qquad (16)$$

which at early times ($t \ll \Delta^{-1}$) approaches a simple gaussian form $G_{zz}(t) \sim \exp[-\Delta^2 t^2]$. The interpretation of Δ is defined by

$$\Delta^2/\gamma_\mu^2 \;=\; \frac{1}{2}\left(\langle B_x^2\rangle + \langle B_y^2\rangle\right); \qquad (17)$$

thus Δ is γ_μ times half the mean squared internal field in the plane perpendicular to the initial muon polarization (taken in this notation to be along the $\hat{z}$ direction).

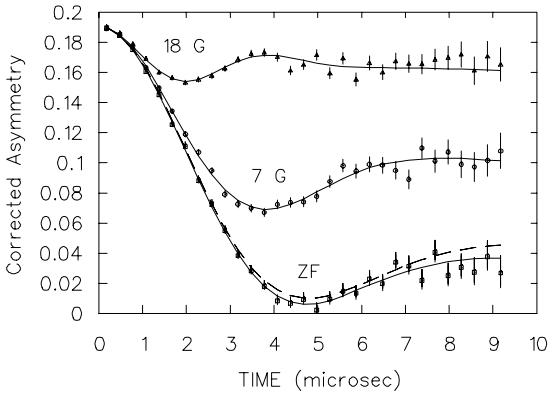

FIG. 18. Zero-field (ZF) and weak (7 and 18 Oe) longitudinal field (wLF)-$\mu^+\mathcal{SR}$ in a single crystal of pure copper at 45 K with the muon polarization initially along the $\langle 111\rangle$ axis of the crystal. At this temperature the muons are almost static in the Cu lattice (hop rate $\lesssim 0.1\ \mu{\rm s}^{-1}$). The solid lines show fits to the exact spin hamiltonian between the muon in an octahedral interstitial site and its six nearest neighbor Cu spins; the dashed line shows a fit to a simple gaussian Kubo-Toyabe function (16).

Motional Narrowing: Figure 18 shows a famous example of nuclear dipolar relaxation of muons in copper metal for ZF and wLF. At the temperature of 45 K the muons are almost perfectly static in the Cu lattice; at higher temperatures they diffuse by thermally activated "hopping" between adjacent octahedral interstitial sites, causing a reduction of the relaxation rate and a change of its shape toward a slow exponential decay (often referred to as "motional narrowing" in reference to the analogous phenomena in NMR where one observes a resonance lineshape whose width is proportional to the relaxation rate). Considerable literature is devoted to

the mathematics of "dynamicizing" static relaxation functions (Kehr, 1978; Hayano *et al.*, 1979; Celio, 1987). At *lower* temperatures the muons again begin to hop as quantum mechanical tunneling becomes important; this phenomenon (and others like it) is an important illustration of quantum diffusion in the presence of dissipation (Luke *et al.*, 1991), a major area of application of $\mu\mathcal{SR}$, which provides a light interstitial probe ideally suited to testing theories of quantum dissipation (Kagan and Klinger, 1974; Kondo, 1986; Yamada, 1986; Kagan and Prokof'ev, 1990; Kagan and Prokof'ev, 1991; Kagan and Prokof'ev, 1992).

Nuclear Dipolar Oscillations: In Fig. 18 we also see a slight difference between the simple Kubo-Toyabe function (16) and the exact quantum mechanical solution of the coupled equations of motion of the muon and its six nearest neighbor Cu spins (Celio, 1986). This reflects the fact that the nuclear moments are not simply static dipoles producing a field at the muon site, but also precess in the dipolar field due to the muon. Such a classical picture quickly becomes useless in picturing the actual evolution of such spin systems, particularly when the nuclei are few in number and have no electric quadrupole interactions, as in the case of the $F\mu F^-$ ion formed when positive muons are implanted into any ionic fluoride compound such as LiF (shown in Fig. 19).

FIG. 19. Zero-field $\mu^+\mathcal{SR}$ asymmetry spectrum in LiF at 89 K, showing the oscillatory behavior of the $F\mu F^-$ ion as a nearly-isolated system of 3 spin-1/2 moments coupled by dipole-dipole interactions. Inset:the rock salt crystal structure showing the μ^+ site (black dot) between two F^- ions (large spheres), which are actually pulled in slightly toward the μ^+ (Brewer *et al.*, 1986).

2.2.4 True Relaxation. In a strong longitudinal field the muon's *spin up* and *spin down* states are good eigenstates of the Zeeman hamiltonian and so the muon polarization will remain static ("locked" by the applied field H) unless some magnetic perturbation drives them in resonance at their Larmor frequency $\omega_\mu = \gamma_\mu H$. Such perturbations with finite spectral density at the muon's Larmor frequency can cause its spin to flip as in magnetic resonance and lead to true relaxation (involving irreversible transitions between energy levels) at a rate T_1^{-1}. For a simple spin-lattice relaxation process with a characteristic correlation time τ_c for fluctuations of local fields of strength δ/γ_μ (whether caused by fluctuations of the fields themselves or by hopping of the muon between sites with different fields) the longitudinal relaxation rate is given

by

$$T_1^{-1} = \frac{2\delta^2\tau_c}{1+\omega_\mu^2\tau_c^2} \qquad (18)$$

which leads to a "T_1 minimum" $T_1(\min) = \omega_\mu/\delta^2$ at $\omega_\mu\tau_c = 1$.

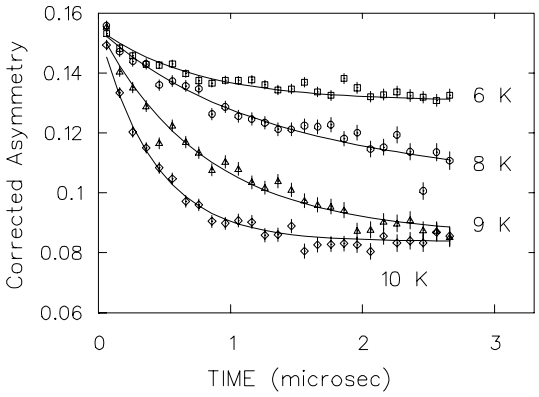

FIG. 20. Longitudinal relaxation of muonium atoms in solid nitrogen at 10 K (diamonds), 9 K (triangles), 8 K (circles) and 6 K (squares) for an applied LF of 8 Oe.

Longitudinal-Field Muonium Relaxation: In very low field, the triplet component of the muonium atom spin system can be treated as a single spin-1 particle with approximately the magnetic moment of an electron. In this case Eq. (18) applies as well for Mu as for the diamagnetic μ^+ (with $\omega_{\rm Mu} \approx 103\omega_\mu$ substituted for ω_μ) and we may see the behavior shown in Fig. 20 as the Mu hop rate τ_c^{-1} changes with temperature.

In higher fields the Mu spin system has 4 eigenstates and transitions among levels become more complicated. Nevertheless an analogous system of rate equations (Yen, 1988) can be used to extract the Mu hop rate as a function of temperature, as shown in Fig. 21. This has allowed precise measurements of the quantum diffusion of muonium in insulators (Kadono, 1990), an important test ground for theories of quantum dissipation (see above).

FIG. 21. (a) Longitudinal relaxation rate T_1^{-1} of muonium atoms in a pure GaAs crystal as a function of field and temperature. (b) The deduced Mu hop rate τ_c^{-1} as a function of temperature. (Schneider *et al.*, 1992)

2.3 Time-Integral $\mu\mathcal{SR}$

In time-integral (I)-$\mu^\pm\mathcal{SR}$ one simply scales the total $e^\pm$ count rate in some direction with no regard for the time of arrival of the muons. As a result, there is no rate limitation: any number of muons may be in the sample at once. As for TD-$\mu\mathcal{SR}$ there are both TF- and LF- versions of I-$\mu\mathcal{SR}$.

2.3.1 Transverse Field I-$\mu\mathcal{SR}$otation. At CW cyclotron accelerators the beam arrives at the production target in few-ns pulses separated by the cyclotron's RF period ($1/\nu_{\rm RF} \sim$ 20-50 ns), which must be stable to high precision. As a result, the muon beam also arrives with the same RF structure, though somewhat smeared out by the pion decay lifetime. If each muon stops in a magnetic field H of just the right strength to match an integer number n of muon spin Larmor precession periods (n/ν_μ) to the RF period, then the polarization of muons arriving in subsequent RF "buckets" will be *in phase* with those arriving previously. Usually n is limited to 1-3 because of the finite width of the muon buckets. The RF period is broken up into a small number of *timing gates* during which muon decays in a given direction (determined by a counter) are accumulated in different scalers. As illustrated in Fig. 22, the rate in a given gate as a function of magnetic field exhibits a resonance as the RF period matches an integer number of Larmor periods. In the absence of spin relaxation the resonance lineshape is Lorentzian with a width of $1/\tau_\mu$ due to the finite muon lifetime; as relaxation is included the lineshape becomes more complicated but may be fitted to a model function. All such resonance lines for the various gates are fitted simultaneously to determine the position and width of the line.

This *stroboscopic* $\mu\mathcal{SR}$ technique was developed to make a precise measurement of the muon's magnetic moment (Camani *et al.*, 1978) and has since been adapted to muon Knight shift measurements (Gygax *et al.*, 1984), where its unlimited rate gives it an advantage over TD-$\mu\mathcal{SR}$ methods. "Strobo-$\mu\mathcal{SR}$," as it is called, is best suited to situations where the muon precesses at a single well-defined frequency and where any relaxation is either uninteresting or fast enough ($\gtrsim$ 0.454 μs^{-1}) to be easily unfolded from the "natural linewidth." Splittings of less than this linewidth cannot be unambiguously resolved by strobo-$\mu\mathcal{SR}$. However, single frequencies (and thus, *e.g.*, muon Knight shifts) can be rou-

FIG. 22. Resonance signals in a *strobo*-$\mu\mathcal{SR}$ experiment (Camani *et al.*, 1978).

tinely measured with a precision of $\lesssim 5$ *ppm* by this method.

2.3.2 Longitudinal Field I-$\mu\mathcal{SR}$elaxation. In ZF and LF the I-$\mu\mathcal{SR}$ technique is much simpler, consisting of simply scaling decay counts in the forward (+) and backward (−) directions separately and measuring the resultant asymmetry as a function of independent variables like magnetic field or temperature. The relevant terms are defined below.

R = rate of arrival of muons

$\epsilon_\pm$ = efficiency of e detector along(+) or opposite(−) μ polarization

$B_\pm$ = backgound rate in said e detector

$A_\pm$ = intrinsic asymmetry of e detector [Count rate $\sim (1 \pm A_\pm)$ for muons fully polarized along (opposite) detector axis of symmetry.]

$G_{zz}(t)$ = longitudinal relaxation function

The number of counts in time $T \gg \tau_\mu$ is

$$N_\pm = B_\pm T + RT\epsilon_\pm \pm RT\epsilon_\pm A_\pm \mathcal{L}(G_{zz}), \tag{19}$$

where $\mathcal{L}(G_{zz}) \equiv \int_0^\infty e^{(-t/\tau_\mu)} G_{zz}(t) \dfrac{dt}{\tau_\mu}$ (20)

is the *Laplace Transform* of $G_{zz}(t)$.

Experimental Asymmetry:

$$\mathcal{A} \equiv \frac{N_+ - N_-}{N_+ + N_-} \qquad \text{or} \tag{21}$$

$$\mathcal{A} = \frac{b_- + (1-\alpha) + (1+\alpha\beta) A_+ \mathcal{L}(G_{zz})}{b_+ + (1+\alpha) + (1-\alpha\beta) A_+ \mathcal{L}(G_{zz})} \tag{22}$$

where $b_\pm \equiv \dfrac{B_+ \pm B_-}{R\epsilon_+}$, $\alpha \equiv \dfrac{\epsilon_-}{\epsilon_+}$, $\beta \equiv \dfrac{A_-}{A_+}$.

Approximations: $B_\pm \approx 0$, $A_\pm \approx A$ and $\epsilon_+ \approx \epsilon_-$,

giving $\alpha \approx \beta \approx 1$, $b_\pm \approx 0$ and

$$\mathcal{A} \approx \frac{(1-\alpha)}{(1+\alpha)} + \frac{2}{(1+\alpha)} A_+ \mathcal{L}(G_{zz}) \tag{23}$$

where $(1-\alpha)/(1+\alpha)$ is the "baseline" asymmetry for totally unpolarized muons.

2.3.3 Avoided Level Crossing Resonance. The LF I-$\mu\mathcal{SR}$ method discards all details of the time dependence of the muon polarization, preserving only the Laplace transform of $G_{zz}(t)$; thus it may appear to be a retrogressive step. Indeed, at a *pulsed* $\mu\mathcal{SR}$ facility, where all the muons arrive at once (within some δt), there is little motive for ignoring the time dependence. However, most muon channels at Meson Factories are able to produce at least an order of magnitude more muons than can be accomodated in a conventional TD-$\mu\mathcal{SR}$ experiment because of the pile-up ambiguity alluded to in an earlier section. Thus I-$\mu\mathcal{SR}$ trades off detailed information for higher sensitivity by accepting the full muon stop rate.

This is particularly useful when one is looking for *conditions of enhanced relaxation*, the most common being those values of the applied magnetic field for which the muon Zeeman splitting matches a transition between energy levels of the nuclear spins, leading to the possibility of

a "flip-flop" of spins in which the muon and the nucleus simultaneously change levels with no change in total energy.

Such conditions are referred to as either "level crossing resonance" (LCR) or "avoided level crossing" (ALC) depending mainly upon one's laboratory affiliation; the two acronyms refer to the same phenomena but one emphasizes the fact that levels never actually cross in quantum mechanics.

Nuclear Quadrupolar μALCR: The first such resonance studied in $\mu\mathcal{SR}$ was actually observed with TD-$\mu\mathcal{SR}$ methods following a suggestion by A. Abragam (Abragam, 1984). In that experiment (Kreitzman *et al.*, 1986), the μ^+ Zeeman splitting at 81 Oe matches the (mostly) electric quadrupolar splitting between $m_I = \pm 3/2$ and $m_I = \pm 1/2$ levels of the spin-3/2 Cu nuclei, causing the resonant relaxation shown in Fig. 23. This measurement and its later improvements (Luke *et al.*, 1991) allowed a precise determination of the electric field gradient produced by the μ^+ at the Cu sites; similar experiments have since revealed nuclear quadrupolar μALCR's in solids containing ^{17}O, ^{14}N and other nuclei. The main application is in determining the muon site in crystals.

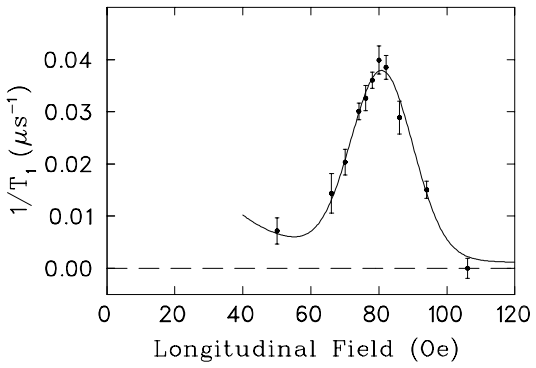

FIG. 23. Longitudinal relaxation rate of muons in a single crystal of copper with the applied field (and the muon polarization) along the ⟨111⟩ crystalline axis (Kreitzman *et al.*, 1986).

"Muonated" Radicals: Shortly after the discovery of nuclear quadrupolar μALCR it was realized that a much stronger resonance could occur through the hyperfine interactions of unpaired *electrons* with both the μ^+ and the nuclear spins. The quantum mechanics of this system is considerably more complicated, but the vague notion of level-matching is still applicable: when the energy difference between two states in which both the muon and the nuclear spins have flipped approaches zero, resonant muon depolarization can occur.

One of the first applications of this principle to *paramagnetic* systems was in the case of the $C_6F_6Mu\cdot$ radical, a paramagnetic molecule formed by addition of a Mu atom to a double bond in the hexafluorobenzene ring (Kiefl *et al.*, 1986). In these measurements a time-integral method is always used, which is sometimes subject to "noise" as beam conditions shift without notice; to combat this problem and produce the smooth resonance patterns shown in Fig. 24, a *field-differential* technique is often employed: the experimental asymmetry $\mathcal{A}$ defined in Eq. (22) is measured for short time intervals (seconds) with a "toggle field" $\pm\delta H$ applied alternately along (+) or opposite (−) the main longitudinal field H_0 and the difference between these two asymme-

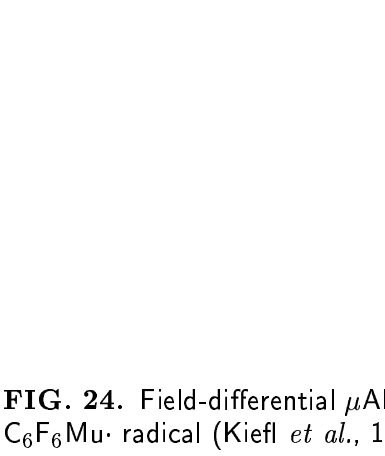

FIG. 24. Field-differential μALCR in the $C_6F_6Mu\cdot$ radical (Kiefl *et al.*, 1986).

tries ($\mathcal{A}^+ - \mathcal{A}^-$) recorded as a function of H_0. This produces a signal analogous to a true differential resonance ($d\mathcal{A}/dH_0$) except that the finite difference ($\pm\delta H$) can actually be larger than the natural width of the resonance in some cases, producing a "bump" followed by a mirror-image "dip" $2\delta H$ later.

Many such radicals have now been studied using this method, resulting in much detailed information about both the structure and the dynamics of these molecules, whose difference from the analogous radicals formed by H atom addition is often insignificant. Several new species never observed in any other way have been discovered using μALCR spectroscopy.

Muonium in Semiconductors: Another paramagnetic system amenable to study by these methods is the muonium-like center in semiconductors, where the unpaired electron may have hyperfine interactions not only with the μ^+ but also with neighboring nuclei of the lattice. The resulting spectroscopy can be very rich, as illustrated in Fig. 25, and reveals the muonium site as well as a great deal of information about its electronic wavefuction. This has been used to obtain most of what is known about isolated atomic hydrogen in Si, GaAs, GaP and CuCl (Kiefl *et al.*, 1992a).

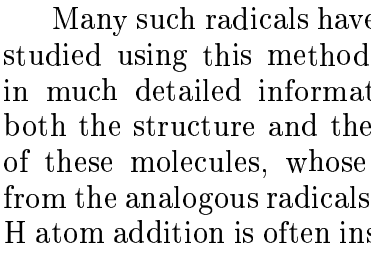

FIG. 25. Muonium-nuclear ALCR spectra in a single crystal of CuCl (Schneider *et al.*, 1990). The Mu^I (low temperature) and Mu^{II} (high temperature) muonium states have the same hyperfine interactions with neighbouring nuclei but slightly different ω_0 values.

2.4 Muon Spin Resonance

Traditional magnetic resonance techniques involve intentional irradiation of the probe spin system with photons of energies equal to transitions between its eigenstates. None of the $\mu\mathcal{SR}$ techniques so far described have involved such irradiation, but true *resonance* techniques are also used in $\mu\mathcal{SR}$, as outlined below. As in NMR, ESR, ENDOR *etc.*, the variety of

irradiation schemes is huge and constantly growing; only a few simple generalizations are possible in limited space.

2.4.1 RF I-$\mu\mathcal{SR}$esonance. The first and most familiar form of muon spin *resonance* uses an RF field in the frequency range of about 5-500 MHz to drive the polarization of muons in diamagnetic states (*i.e.*, "bare" muons) in resonance at fields of 300 Oe to 4 T. The RF field may be generated in a simple coil at the lower frequencies or a cavity at the higher. In some cases the RF frequency can be swept through resonance, but most often the main field H_0 is swept, as in NMR. A good recent survey of these techniques and applications may be found in (Nishiyama *et al.*, 1992).

For the higher frequencies the same apparatus may be used at lower fields to study paramagnetic species such as muonated radicals. An interesting variation of this is seen in Fig. 26.

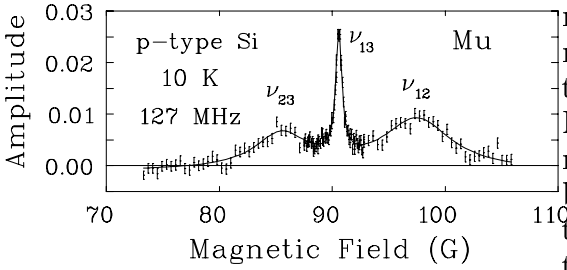

FIG. 26. Muonium resonance in mildly p-type Si at 10 K in a 127 MHz RF field, showing power-broadened resonances at the two muonium transition frequencies ν_{12} and ν_{23} (see Fig. 13) as well as a sharp two-photon resonance at the ν_{13} frequency.

The time scale for muon spin resonance is restricted by the muon lifetime; to be observed, a resonance effect must affect the muon polarization in $\lesssim 10$ μs, implying an RF field $H_1 \gtrsim 2$ Oe, which is not difficult to achieve but represents fairly high RF power. Because of power supply limitations and Ohmic heating, such irradiations are less efficient at CW facilities than at pulsed-beam facilities (Nishiyama *et al.*, 1992), where all the muons can be irradiated simultaneously with timed bursts of RF power; nevertheless, RF-$\mu\mathcal{SR}$ is quite feasible at CW facilities (Kreitzman *et al.*, 1990) and has enjoyed a rapid growth of applications virtually everywhere.

One advantage of RF-$\mu\mathcal{SR}$ is that it can identify *final states* of muons in situations where stochastic processes render impossible the usual means of identification of these states by their distinctive time spectra. A typical example is the *delayed formation* of diamagnetic molecules following initial formation of Mu atoms: in TF-$\mu\mathcal{SR}$ the early Mu precession quickly dephases the muon polarization so that no signal can be seen from the diamagnetic final state unless the reaction times are short compared to the Mu frequency; in strong LF, however, not only is the Mu polarization "held" by the applied field but the population of the final state as a function of time can be determined by delaying the RF pulse (at the diamagnetic resonance frequency) relative to the time of arrival of the muons.

Perhaps the most exciting feature of RF-$\mu\mathcal{SR}$ is its ability to reveal the time evolution of the muon polarization *during* the RF irradiation, a capability denied to conventional magnetic resonance techniques which

detect the same sort of electromagnetic signal as they use to drive the probe spins. This is a consequence of the fact that $\mu^+\mathcal{SR}$ detects high energy positrons whose registration by the counters is unaffected by the RF fields.

2.4.2 Muon Spin Echoes. Many modern NMR techniques involve *pulses* of RF power designed to rotate the probe's polarization through various angles in the rotating reference frame. This is more difficult for muons because of their short lifetime — to be useful in $\mu\mathcal{SR}$ a $\pi/2$ pulse must be no more than $\lesssim 1$ μs long, which means an RF magnetic field of $H_1 \gtrsim 75$ Oe. This is barely possible with today's RF techniques. It is particularly difficult at CW facilities, where the RF pulse must be *asynchronously triggered* by the arrival of individual muons, in order to occur at the same time (relative to "$t = 0$" when the muon arrives in the sample) for each. Nevertheless, such *spin echo* techniques (nicknamed μSE) were first successfully demonstrated at TRIUMF, a CW facility (Kreitzman *et al.*, 1988).

As mentioned earlier, $\mu\mathcal{SR}$ detection techniques allow observation of the time evolution of the muon polarization *during* the RF irradiation. This can be especially informative in the case of μSE pulse sequences. An example is shown in Fig. 27.

A bonus of RF-$\mu\mathcal{SR}$ at pulsed facilities is the chance to overcome the *time resolution* limitations of pulsed beams (muons arrive in bunches $\gtrsim$ 50 ns long) by stopping the muons in a strong LF and then using a high-power phase-locked $\pi/2$ pulse to rotate them all *in phase* into the plane perpendicular to $\vec{\mathbf{H}}_0$, after which they will exhibit HTF-$\mu\mathcal{SR}$ precession with all the same observables as enjoyed at CW facilities.

FIG. 27. Muon spin echo in the rotating reference frame during a $(\Pi/2)_y$-τ-Π_y pulse sequence (shaded regions) where the muons arrive initially polarized along $\vec{\mathbf{H}}_0 = H_0\hat{z}$ and the detectors are in the $\hat{x}$ and $\hat{y}$ directions. The small signal observed along the $\hat{y}$ axis indicates that the RF was slightly off resonance. The inset shows the geometry of the positron detectors and the polarization during the $\Pi/2$ pulse. (Kreitzman *et al.*, 1988).

3. $\mu\mathcal{SR}$ APPLICATIONS

Examples of selected experimental results having been shown above, this section will focus mainly on the "scientific demography" of $\mu\mathcal{SR}$.

3.1 Muonium Chemistry

One of the main themes of $\mu\mathcal{SR}$ could be characterized as "The Chemistry of a Light Isotope of Hydrogen." The muonium atom and the H atom have the same size, almost the same reduced mass and ionization potential, and both obey the Born-Oppenheimer approximation (the electron wavefunctions adiabatically adjust to the slow motions of the nuclei) that allows relatively simple calculations of chemical reaction processes and molecular structure.

3.1.1 Chemical Kinetics. This strong similarity, combined with the unprecedented *isotopic* difference (a ratio of ~ 18 in mass between Mu and D) and the enhanced quantum behaviour of the light Mu atom, make muonium chemistry a very important testing ground for the few *ab initio* theories of chemical reaction kinetics (Fleming *et al.*, 1992).

Once the *differences* between Mu and H chemistry are well understood (as is now the case for many types of reactions), measurements of Mu reactivity (which are often easy) can be used to reliably predict the reactivity of H under circumstances where H atoms cannot even be detected. This is now entirely feasible but has not yet attracted much attention from the "practical" side of the chemistry community.

3.1.2 Radicals. Following chemical reaction, Mu is often incorporated into *radicals* (molecules with unpaired electrons) where a weakened hyperfine interaction persists between the electron and muon spins (and also between the electron and any other nuclei with magnetic moments). These molecules resemble their hydrogenic analogues (where the μ^+ is replaced by a proton) so closely that most of their reaction kinetics are nearly identical. This allows use of the "muonated" version to learn the chemical behaviour of the "protonated" version even when information on the latter is unavailable by other methods. In some cases, $\mu\mathcal{SR}$ has confirmed the very *existence* of radicals that have never been observed by any other means.

3.1.3 Molecular Structure. By using μALCR techniques one can use $\mu\mathcal{SR}$ to measure not only the hyperfine coupling of the muon to the unpaired electron but also the couplings of that electron to the *other* nuclei; thus the muon can be used to read out the molecular structure of regions of the molecule quite far from the muon's site, much as in a conventional ENDOR experiment (Percival *et al.*, 1987). The details of the *structure* of muonium- and hydrogen-substituted versions of radicals are sometimes influenced by the lighter mass of the muon: bond lengths to Mu tend to be slightly longer and bond angles are often changed by the larger zero-point motions of Mu. This, combined with the fact that the nuclear hyperfine couplings can often be measured more accurately by $\mu\mathcal{SR}$ than by ENDOR, makes μALCR a very important probe of molecular structure (Roduner, 1988).

3.2 Condensed Matter Physics

The applications of $\mu\mathcal{SR}$ in condensed matter physics also include

many comparisons between the μ^+ and the proton, insofar as their behaviours in matter differ only by virtue of the muon's lighter mass; however, there are perhaps a greater variety of applications that might be titled, "The Muon as a Magnetic Probe." Both types will be surveyed briefly below.

3.2.1 Hydrogen in Semiconductors. Closely related to the muonium chemistry applications discussed above are the uses of $\mu^+\mathcal{SR}$ to learn the location, electronic structure and dynamical behavior of Mu and/or H atoms in semiconductors, where H is known to be an ubiquitous impurity but where far more is known about isolated H atoms from $\mu\mathcal{SR}$ than from any method that observes H itself (Patterson, 1988, Kiefl *et al.*, 1988). Since H is known to affect the electronic properties of Si and GaAs and is now being used specifically for the purpose of *passivation* of electrically active impurities, this knowledge is vital to the semiconductor industry; consequently, $\mu^+\mathcal{SR}$ spectroscopy in semiconductors is one of the most important applications of $\mu\mathcal{SR}$ in solids. Figure 28 shows the temperature dependence of the probability of finding the muon in an ionized state (either μ^+ or Mu^-) at times comparable to the muon lifetime (long after any initial formation or reaction of paramagnetic states), obtained by RF-$\mu\mathcal{SR}$ at the diamagnetic frequency. Comparison of these results with those for highly doped p- or n-type Si reveals the interactions between H-like species and impurities

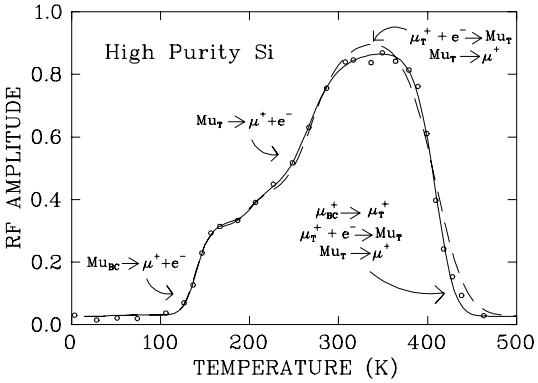

FIG. 28. The RF-$\mu^+\mathcal{SR}$ diamagnetic resonance amplitude in pure silicon, showing evidence for thermally activated transitions between various charge states and lattice sites of the μ^+: Mu_{BC} = "anomalous" muonium (also called Mu*) localized at a Si-Si bond-centred site; Mu_T = quasi-free Mu atom diffusing rapidly between tetrahedral sites; μ^+_{BC} and μ^+_T indicate freshly-ionized muons at the corresponding sites (Hitti *et al.*, 1994).

(Hitti *et al.*, 1994).

3.2.2 Quantum Diffusion. As mentioned earlier, the theory of *quantum dissipation* (quantum tunneling or bandlike propagation in the presence of stochastic or other interactions with the host medium) is currently a very important field of condensed matter physics, having implications for the electronic and diffusive transport properties of all types of materials (Stamp and Zhang, 1991; Kagan and Prokof'ev, 1992). Because of its light mass, its affinity for electrons and its repulsion from nuclei, the μ^+ (and its neutral version, Mu) is an apt probe of such behavior, the ideal "light interstitial." (Flynn and Stoneham, 1970; Kagan and Klinger, 1974; Petzinger, 1982)

Study of the *quantum diffusion* of μ^+ and Mu in solids has therefore comprised a significant fraction of the $\mu\mathcal{SR}$ community's experimental effort over the last two decades (Kadono, 1992) and the results of such experiments have attracted considerable theoretical interest (Kagan and Prokof'ev, 1992).

Motion of the μ^+ in Metals: In impure or imperfect metallic crystals, the μ^+ tends to trap at defects or at least be localized in their vicinity; the resultant temperature dependence of motional narrowing effects, used to measure μ^+ mobility, can be quite complicated (Moslang *et al.*, 1983; Petzinger, 1982). In pure, well-annealed crystals, however, one often observes the intrinsic interactions between the μ^+ and the lattice. The hopping of positive muons in various pure metals has been studied extensively by means of ZF- and wLF-$\mu^+\mathcal{SR}$ measurements such as those shown in Fig. 18 (Luke *et al.*, 1991) as well as by TF-$\mu^+\mathcal{SR}$ motional narrowing experiments. These studies have revealed a qualitatively consistent temperature dependence typified by the classic example shown in Fig. 29: at high temperatures (above about 80 K in the case of Cu) the muon exhibits semiclassical thermally activated hopping over the energy barriers between adjacent interstitial sites; at lower temperatures (below about 20 K for Cu) the μ^+ actually hops *faster* as T *decreases*, due to the increasing probability of quantum tunneling between sites, as the disorder due to lattice vibrations is reduced. The power law $\tau_c^{-1} \propto T^{-\alpha}$ is predicted by theory (Kondo, 1992) to have a much smaller exponent α for screened positive muons in metals than in insulators, due to the additional dissipation in electronic degrees of freedom (often referred to as "electron drag" effects). At still lower T the intrinsic disorder of even pure high quality crystals begins to inhibit tunneling once again. Similar results have been observed in aluminum using indirect methods involving trapping of the μ^+ at impurities.

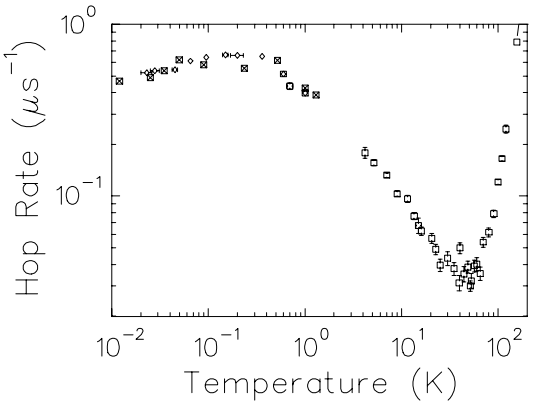

FIG. 29. Temperature dependence of the μ^+ hop rate τ_c^{-1} in pure copper crystals (Luke *et al.*, 1991).

Muonium Diffusion in Nonmetals: In ionic crystals, the μ^+ tends to form a hydrogen bond with the most negative species in the lattice, such as F^- or O^{--} ions. Muon diffusion is thus suppressed until quite high temperatures, typically $-sim200$ K (Kiefl *et al.*, 1990). If the muon forms muonium, however, the Mu atom is more or less decoupled from local electric fields and usually diffuses freely through the lattice; interestingly, Mu diffusion is quite similar in both covalent and ionic nonmetals. An example of Mu diffusion in the semiconductor GaAs was shown earlier in 21 (Schneider *et al.*, 1992); a startlingly similar

result was obtained (Kiefl *et al.*, 1989) in an ionic insulator (KCl), as shown in Fig. 30. Somewhat different Mu

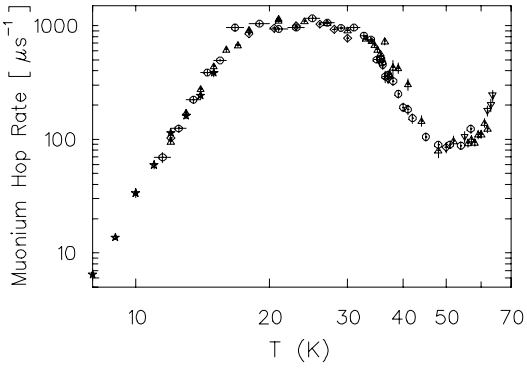

FIG. 31. Temperature dependence of the muonium hopping rate in solid nitrogen cryocrystals (Storchak *et al.*, 1994).

FIG. 30. Temperature dependence of Mu hop rate in KCl (Kiefl *et al.*, 1989).

hopping behaviour is observed in the Van der Waals insulator s-N_2 formed by crystallization of solid nitrogen, as shown in Fig. 31. Such so-called *cryocrystals* have very low Debye temperatures and quite weak couplings between the neutral Mu atom and the host lattice; they are therefore interesting systems in which to test theoretical predictions of the temperature dependence of Mu quantum diffusion (Storchak *et al.*, 1994). An interesting effect has been observed in *superconducting aluminum*, which can be driven normal by an applied magnetic field: at the same T, muon diffusion is considerably *faster* in the superconducting (SC) state than in the normal state, because the opening of a SC gap at the Fermi surface effectively quenches the dissipation due to screening electrons (Kondo, 1992). Thus SC Al acts like an insulator with respect to muon quantum diffusion.

3.2.3 Magnetism. Perhaps because it so easily generates rich and precise data, *magnetism* is currently the largest area of application of $\mu\mathcal{SR}$.

In magnetically ordered materials the muon (μ^+ or μ^-) generally samples the local magnetic field at some preferred site or sites and reveals that field through its characteristic Larmor precession frequency (Seeger and Schimmele, 1992). The local field $\vec{\mathbf{B}}_\mu$ is composed of several contributions:

$$\vec{\mathbf{B}}_\mu = \vec{\mathbf{H}}_0 + \vec{\mathbf{B}}_\mathrm{L} + \vec{\mathbf{B}}_\mathrm{dip} + \vec{\mathbf{B}}_\mathrm{HF} \qquad (24)$$

where $\vec{\mathbf{H}}_0$ is the externally applied field (if any), $\vec{\mathbf{B}}_\mathrm{L}$ is the *Lorentz field* produced by magnetic "charges" induced on the interior of a hypothetical spherical cavity around the muon site due to the average bulk magnetization of the medium, $\vec{\mathbf{B}}_\mathrm{dip}$ is the *dipolar field* due to all the microscopic moments within the Lorentz cavity and $\vec{\mathbf{B}}_\mathrm{HF}$ is a *hyperfine field* transmitted to the muon by its Fermi contact interactions with conduction electrons. The last two components are usually the focus of experiments on magnetically ordered systems, where $\vec{\mathbf{B}}_\mu$ is

usually measured with $\vec{\mathbf{H}}_0 = 0$, as well as measurements of the muon Knight shift $K_\mu \equiv (B_\mu - H_0)/H_0$ in paramagnets.

Interpretation of these fields requires a knowledge of the muon site, including zero-point motion and any tunneling between nearby sites, and can be quite difficult; nevertheless, in many cases it is easier than trying to sort out the "core polarization" effects of various interacting atomic electrons that transmit the hyperfine field to the nucleus in (*e.g.*) NMR.

One attractive feature of $\mu\mathcal{SR}$ in magnetism studies is that measurements of internal magnetic fields can be performed on unaligned polycrystalline or powdered samples almost as easily as on perfect single crystals. In zero applied field, if all the local fields have the same *magnitude*, the only effect of random *directions* is to reduce the muon precession amplitude to 2/3 of the value that would be observed if the fields were all perpendicular to the muon polarization. Thus ZF-$\mu\mathcal{SR}$, which requires a minimum of apparatus, is often adequate for very detailed investigations of the temperature dependence of magnetic order and dynamics. Moreover, using ZF-$\mu\mathcal{SR}$ one can measure B_μ in crystals exhibiting antiferromagnetism or even more exotic forms of magnetic order as easily as in simple ferromagnets. A classic example is shown in Fig. 32 for the intermetallic compound MnSi, where the magnetic field due to itinerant electron moments forms a long-wavelength spiral with a small component along the axis of the spiral — so-called *helimagnetic* order.

Disordered magnetic systems (such as *spin glasses*) can also be studied rather easily by $\mu\mathcal{SR}$, leading to a strong $\mu\mathcal{SR}$ presence in the currently popular area of frustrated and low-dimensional magnetism. A classic example is shown in Fig. 33 and a more recent case in Fig. 34.

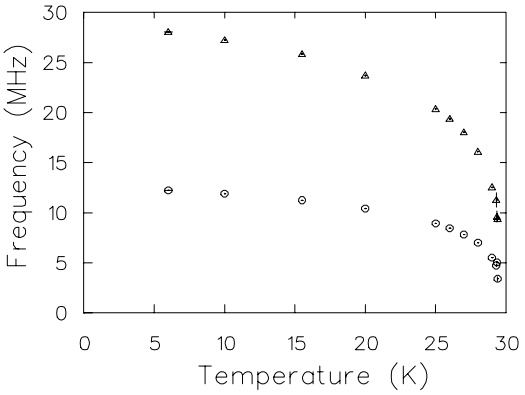

FIG. 32. Temperature dependence of the magnitudes of the internal fields at two different μ^+ sites in a single crystal of the itinerant helimagnet MnSi.

FIG. 33. Comparision of neutron spin echo (NSE), ZF-$\mu\mathcal{SR}$ and ac-susceptibility measurements on the spin glass CuMn(5 at.%), showing the time dependence of the static order parameter ξ (related to the fraction of Mn moments that have not yet moved appreciably) at several temperatures *below* the nominal glass transition at $T_g = 27.4$ K (Uemura *et al.*, 1984).

3.2.4 Superconductivity.

Because muon decay provides a non-electromagnetic "signal," $\mu\mathcal{SR}$ is able to probe magnetic fields inside superconductors without distortion. This gives $\mu\mathcal{SR}$ a unique window on the magnetic behaviour of superconductors. Since 1987 the $\mu\mathcal{SR}$ community has exploited this advantage in the study of high temperature superconductors (HTSC).

Phase Diagrams: All of the copper oxide superconductors show either antiferromagnetic (AFM) or spin glass-like (SGL) order very close to (and sometimes overlapping) the superconducting (SC) phase, as first demonstrated for $YBa_2Cu_3O_x$ by $\mu\mathcal{SR}$ experiments in 1988. Since then the temperature *vs.* doping phase diagrams of most HTSC materials have been mapped out using $\mu\mathcal{SR}$.

Magnetic Penetration Depth: The first application of $\mu\mathcal{SR}$ to HTSC was in measuring the magnetic penetration depth λ by fitting the high transverse field (HTF)-$\mu\mathcal{SR}$ time spectrum to a simple gaussian relaxation function and thus estimating the second moment of the frequency distribution due to the vortex lattice of magnetic flux penetrating a type II superconductor in the mixed state. Figure 35 shows the earliest results, obtained in January 1987 (Aeppli *et al.*, 1987). Since then an enormous body of data has been accumulated by this method, which is still the most reliable way to estimating λ in sintered, random powders. However, as evident in Fig. 11, for well-characterized single crystals one finds a lineshape much less symmetric than a gaussian, as predicted by London and later Gorkov models of the vortex lattice. The ability to make such measurements and interpret them correctly in terms of λ and ξ is a recent achievement of $\mu\mathcal{SR}$, which is now poised to exploit these capabilities to legitimize (or, in some cases, debunk) the many published $\mu\mathcal{SR}$ results worldwide interpreting the gaussian-fitted linewidths (for sintered powder or aligned HTSC samples) in terms of λ.

Universal Correlations between T_c and n_s: A collection of such results has been assembled by Y.J. Uemura to produce the plot shown in Fig. 36, commonly known as an "Uemura

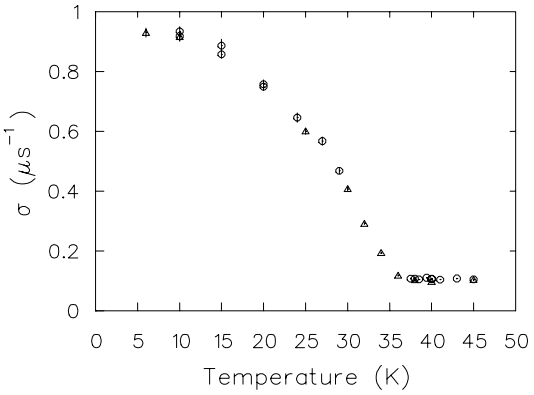

FIG. 34. Muon spin relaxation rate T_1^{-1} due to fluctuating local fields in the antiferromagnetically frustrated two-dinensional *Kagomé lattice* (shown inset) of $SrCr_8Ga_4O_{19}$ (Uemura *et al.*, 1994). The increase of T_1^{-1} with decreasing T is a manifestation of the gradual slowing down of Cr spin fluctuations; the saturation of this effect below T_g shows that the Cr moments never freeze even as $T \to 0$. This is in marked contrast with the situation in dilute spin-glasses like CuMn, where all fluctuations cease as $T \to 0$.

FIG. 35. First TF-$\mu^+\mathcal{SR}$ measurement of the temperature dependence of the μ^+ dephasing rate σ (proportional to λ^{-2}, the inverse square of the magnetic penetration depth, which is in turn proportional to the superconducting carrier density n_s) in a high-T_c cuprate superconductor — in this case an unaligned sintered powder sample of $La_{1.85}\mathcal{SR}_{0.15}CuO_4$ in an applied field of 0.4 T (Aeppli *et al.*, 1987).

plot." (Uemura *et al.*, 1989) The "universal" linear dependence of T_c on n_s in the *underdoped* (less than optimal n_s) regime gives way to a "turnover" and eventual linear *decrease* of T_c with increasing n_s in the *overdoped* regime (Niedermayer *et al.*, 1993).

Non-s-Wave Pairing? Whether it be crudely characterized in terms of a gaussian relaxation rate σ or more accurately represented by the second moment of a lineshape, the muon dephasing rate due to the vortex lattice in a type II superconductor is proportional to the inverse square of the London penetration depth, λ^{-2}, which in turn is proportional to the superconducting carrier density n_s. Thus a measurement of the temperature dependence of σ is (apart from a normalization) also a measurement of the excitation of normal carriers across the superconducting energy gap which characterizes the pairing mechanism. A conventional BCS "s-wave" superconductor has a prescribed T-dependence of n_s, variations from which are taken as evidence for unconventional pairing mechanisms. While all this should, in the author's opinion, be taken with a grain of salt, still $\mu\mathcal{SR}$ has been an important contributor to the debate over the still-mysterious mechanism for HTSC. While the $\mu\mathcal{SR}$ data for the 18 K superconductor K_3C_{60} are consistent with s-wave BCS superconductivity, the $\mu\mathcal{SR}$ results on certain organic and heavy-fermion su-

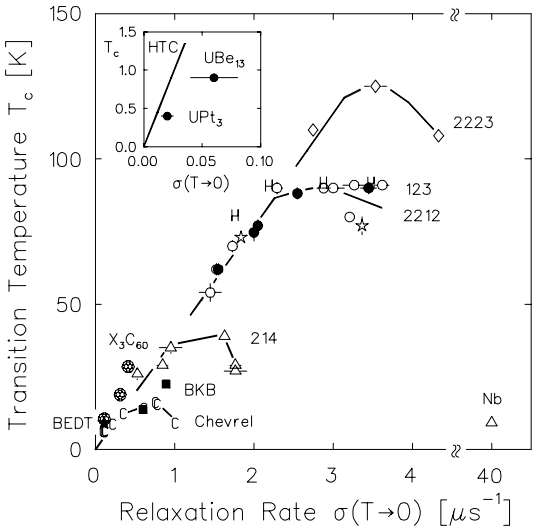

FIG. 36. Correlations between the superconducting carrier density n_s (as measured by the μ^+ dephasing rate σ) and the superconducting transition temperature T_c for a wide variety of "exotic" superconductors including many HTSC; conventional BCS superconductors have higher n_s with lower T_c.

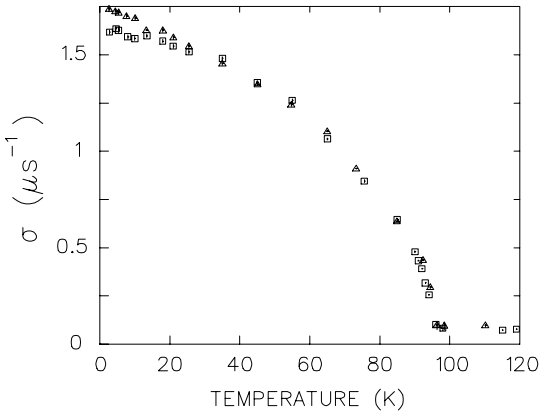

FIG. 37. Temperature dependence of the μ^+ dephasing rate σ (proportional to the superconducting carrier density n_s) in single crystals of $YBa_2Cu_3O_{6.95}$ in a TF-$\mu^+\mathcal{SR}$ experiment at 0.5 T (triangles) and 1.5 T (squares). An "s-wave" BCS superconductor is expected to show very weak T-dependence near $T = 0$; in contrast, these data indicate an almost linear decrease from $T = 0$.

perconductors show a T-dependence strongly suggestive of nodes in the gap [momentum-space directions in which the superconducting gap vanishes] (Uemura *et al.*, 1992). A very similar T-dependence has been observed for n_s in various samples of $YBa_2Cu_3O_{6.95}$ — most notably in high-quality single crystals — as shown in Fig. 37.

4. $\mu\mathcal{SR}$ FACILITIES

No practical guide to $\mu\mathcal{SR}$ would be complete without some discussion of the *logistics* of $\mu\mathcal{SR}$ experiments and the *facilities* required for its pursuit.

4.1 Logistics of Accelerator Experiments

Because $\mu\mathcal{SR}$ requires muons, which must be produced by large, high-intensity accelerators, $\mu\mathcal{SR}$ beam time will probably always be a scarce commodity for which users will compete fiercely. Such competition has a beneficial effect on the quality of the resulting research, but the scarcity of muons does regulate the growth of the field. It will probably always be the case that $\mu\mathcal{SR}$ experiments will be screened in advance by peer review committees and allocated beam time every few months for periods ranging from a few days to several weeks. While this sort of schedule may often hamper spontaneity, it is well matched to the cycle of experimental conception,

design, execution, data analysis and publication, as evidenced by the high output of most $\mu\mathcal{SR}$ facilities.

Furthermore, because a typical $\mu\mathcal{SR}$ experiment involves so many diverse technologies (from magnetic beam optics to charged particle detectors to magnets and cryostats to fast electronics and extensive on-line computer software) it makes an excellent training ground for students, who, once having mastered the techniques of $\mu\mathcal{SR}$, can apply them almost unaltered to a wide variety of scientific topics.

4.2 Standard $\mu\mathcal{SR}$ Hardware

Most accelerator laboratories with $\mu\mathcal{SR}$ programs also maintain some sort of *$\mu\mathcal{SR}$ user facility* providing standard $\mu\mathcal{SR}$ spectrometers, electronics and data acquisition computers; it is now rare for individual experimental groups to provide their own equipment except for specialized cryostats, ovens, sample cells or data analysis software. Some of the standard components to be found at most $\mu\mathcal{SR}$ user facilities are listed below.

4.2.1 Detectors. The workhorse of $\mu\mathcal{SR}$ is the plastic scintillation counter, in which a flash of light (generated as an ionizing particle passes through the scintillating plastic) is transmitted down clear plastic light guides by total internal reflection to a photomultiplier tube that in turn emits an electrical pulse which is transmitted down a coaxial cable to a fast timing discriminator module in the counting room outside the experimental area (from which experimenters are excluded while the beam is on, due to the appreciable radiation levels in the muon beam itself). The result is a logical timing pulse whose arrival time corresponds within $\sim$ 1 ns (and a fixed delay) to the time the particle passed through the detector. The M and E detectors in Fig. 1 would normally be plastic scintillation counters for the incoming muon and outgoing positron, respectively, and would normally provide a resolution of 0.5-2 ns on the corresponding time interval. With careful design of the counters, special photomultiplier tubes, cables and fast electronics it is possible to achieve time resolutions $\sim$ 100 ps (Holzschuh, 1983; Keller *et al.*, 1987), but this is not yet common.

While scintillation counters are simple, reliable, versatile and have excellent performance in the time domain, they have a number of frustrating features: First, even if the scintillator itself is small the light guides are bulky and inflexible (flexible fibre optics can be used but so far only at the expense of timing degradation and/or loss of light collection efficiency); this becomes increasingly inconvenient as increasing stopping luminosity reduces the scale of $\mu\mathcal{SR}$ samples and experiments. Second, most photomultiplier tubes are very sensitive to magnetic fields and must be magnetically shielded and/or removed to field-free regions by long light guides which again reduce time resolution. Third, scintillation counters have only crude position sensitivity, which is generally of secondary importance to $\mu\mathcal{SR}$ experiments, but could be useful. For example, by distinguishing one incoming muon from

another and matching the outgoing positrons to the muons from which they arise, one may overcome the pile-up rate limitation normally imposed by allowing only one muon in the sample at a time; this technique has been demonstrated but never widely applied.

Potentially promising alternatives include modern proportional counters and solid-state barrier detectors, but neither of these have the required time resolution in their standard configurations; more development work is needed.

4.2.2 Electronics. Raw counter pulses are fed to fast discriminators — usually constant fraction discriminators (CFDs) — which generate uniform timing logic pulses if the raw pulse height is above a set threshold. The logic pulses are processed by a simple "fast electronics" circuit shown schematically in Fig. 38.

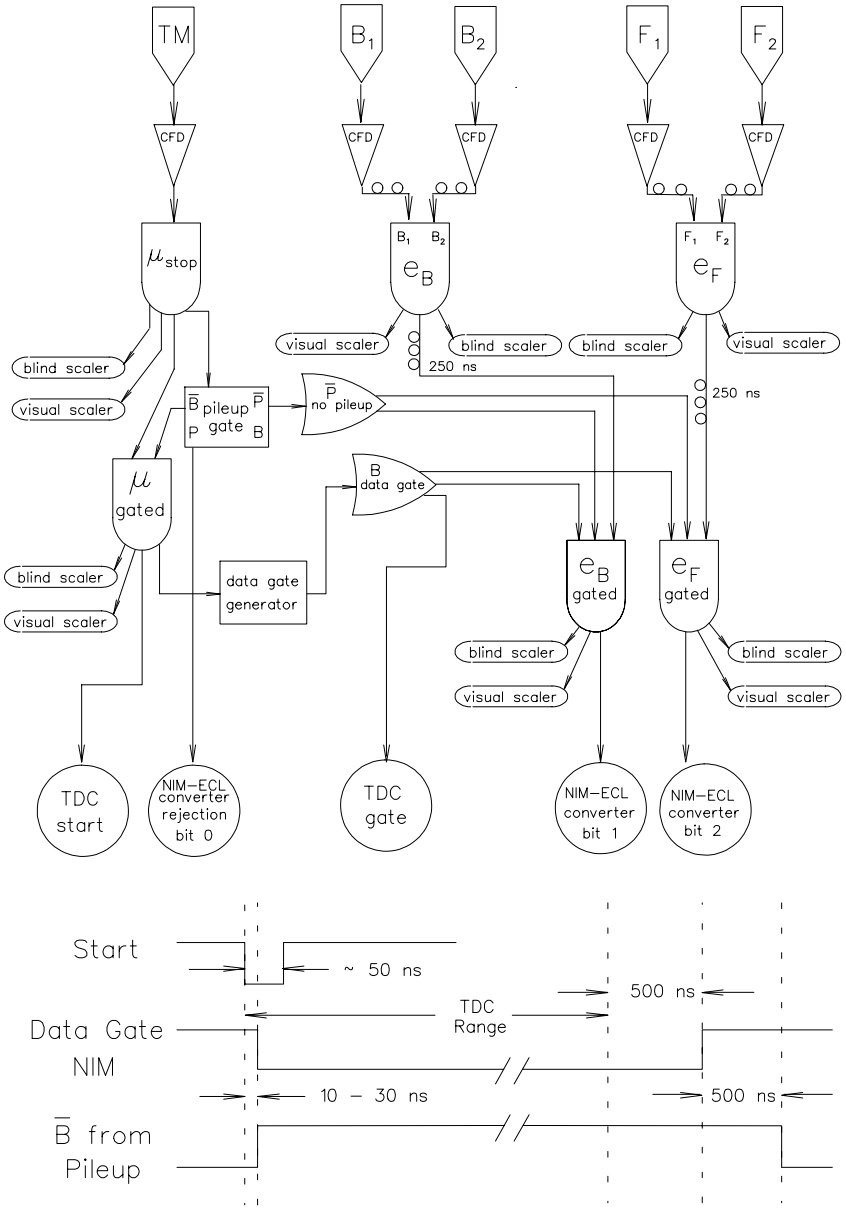

FIG. 38. Schematic electronics logic diagram for two "channels" of a typical time-differential (TD)-$\mu\mathcal{SR}$ experiment (see Fig. 1).

The incoming muon generates a pulse in the M counter which ultimately sends a *start* pulse to a fast time digitizer ("clock"); later the muon decays, triggering a *stop* pulse in the E counter, which stops the clock; the time interval is digitized and the corresponding bin in a time histogram is incremented. The additional logic modules ensure that events with "second muons" are rejected with uniform efficiency throughout the *gate* T, lest rate-dependent distortions spoil the resultant time spectra (histograms) which are the final output of the experiment.

Similar care must be taken to re-

ject "second E" events in which a (possibly accidental) count in an E counter renders the identity of the stop pulse ambiguous. This function is handled internally in the LRS 4204 TDC, which is now the standard $\mu\mathcal{SR}$ clock primarily because it provides this function along with excellent time resolution and the ability to directly increment time bins in a CAMAC Histogramming Memory, thus relieving the data acquisition computer of all event-processing duties except periodic histogram and scaler readout.

There are numerous improvements and adaptations of this basic TD-$\mu\mathcal{SR}$ arrangement, of course, as well as several entirely different electronics setups for time-integral (I)-$\mu\mathcal{SR}$ techniques.

4.2.3 $\mu\mathcal{SR}$ Spectrometers. The local facility almost always supplies a choice of several $\mu\mathcal{SR}$ spectrometers, whose function is to control the magnetic field at the sample (usually by means of three orthogonal sets of Helmholtz coils, one of which can generate a large main field) and to provide mounting brackets for counters, cryostats or other paraphernalia. Often a standard set of counters are an integral part of the spectrometer as well. There is such a huge variety of such spectrometers that it would be pointless to try to describe a "typical" version in any detail.

4.2.4 Target Vessels and Cryostats. Since the muon's initial polarization is independent of the state of its environment, $\mu\mathcal{SR}$ samples may be gases, liquids or solids at any temperature, pressure, magnetic or electric field. This versatility is reflected in the variety of sample environments (target vessels) used in $\mu\mathcal{SR}$ experiments, ranging from large "gas cans" (for studying hydrogen gas at low pressure and high temperature) to miniaturized cryostats (for studying small crystals at low temperature and high magnetic field). The most common use of $\mu\mathcal{SR}$ is currently in low-temperature condensed matter physics, so that most $\mu\mathcal{SR}$ spectrometers have general-purpose cryostats built in (but removable). However, in general the user is responsible for the sample environment.

4.3 $\mu\mathcal{SR}$ Software

Because $\mu\mathcal{SR}$ data is always intimately connected with computers (indeed, one needs computer graphics just to see what one is measuring) and because there is such a premium on efficient use of beam time, which in turn demands that one know what one has learned from one run before setting the independent variables for the next (it is not unusual for a $\mu\mathcal{SR}$ experimenter to generate, while a spectrum is still accumulating, the figures that will be published later to describe it), one of the most important components of any $\mu\mathcal{SR}$ user facility is a suite of process control, data presentation and analysis software to provide the user with all the mathematical tools described in this article, and more. Since implementation of such utilities is nontrivial, some effort is now being made to define international standards (data formats, process control, data analysis *etc.*) so that the $\mu\mathcal{SR}$ community can cooperate on such software development and share the benefits thereof.

5. SPECULATIONS

The felicitous history of $\mu\mathcal{SR}$ has reached a point of crisis in the 1990's: accelerator facilities rarely capture the fascination of the subatomic physicists who build them for more than about two decades, and the Meson Factories have reached that difficult age. While $\mu\mathcal{SR}$ facilities require only modest investments for qualitative improvements using existing accelerators, the big machines themselves need expensive upgrades to maintain world-class status as subatomic facilities. Thus the future of $\mu\mathcal{SR}$ remains inextricably linked to that of subatomic physics — more specifically, to that of high intensity, intermediate energy, fixed-target hadron accelerators. This has always been the case and will remain so until someone invents a tabletop device capable of generating muon beams. In spite of the implied mutual liability, the author has always considered this unlikely symbiosis to be one of the greatest charms of $\mu\mathcal{SR}$.

List of Works Cited

μSR Newsletter **1**, 15 January (1974).

A. Abragam, *C.R. Acad. Sci. Ser. 2* **299**, 95 (1984).

G. Aeppli *et al.*, *Phys. Rev. B* (Brief Reports) **35**, 7129 (1987).

J. Brewer *et al.*, *Phys. Rev. Lett.* **31**, 143 (1973).

J. Brewer *et al.*, *Phys. Rev. A* **9**, 495 (1974).

J. Brewer, *Hyperfine Int.* **8**, 831 (1981).

J. Brewer, *Hyperfine Int.* **17-19**, 879 (1984).

J. Brewer, *Hyperfine Int.* **17-19**, 873 (1984).

J. Brewer *et al.*, *Phys. Rev. B* (Rapid Comm.) **33**, 7813 (1986).

T. Bowen, *Physics Today* **38**, 22 (1985).

M. Camani *et al.*, *Phys. Lett. B* **77B**, 326 (1978).

M. Celio, *Phys. Rev. Lett.* **56**, 2720 (1986).

M. Celio, *Helv. Phys. Acta* **60**, 600 (1987).

F. Combley, F. Farley, and E. Picasso, *Phys. Rep.* **68**, 93 (1981).

J. Cronin, *Revs. Mod. Phys.* **53**, 373 (1981).

P. D. de Réotier, A. Yaouanc, and S. Meshkov, *Phys. Lett. A* **162**, 206 (1992).

E. Fermi and E. Teller, *Phys. Rev.* **72**, 399 (1947).

V. Fitch, *Revs. Mod. Phys.* **53**, 367 (1981).

D. Fleming and M. Senba, in "Perspectives of Meson Science", eds. T. Yamazaki, K. Nakai and K. Nagamine 219 (1992).

C. Flynn and A. Stoneham, *Phys. Rev. B* **1**, 3966 (1970).

J. Friedman and V. Telegdi, *Phys. Rev.* **105**, 1681 (1957).

R. Garwin, L. Lederman, and M. Weinrich, *Phys. Rev.* **105**, 1415 (1957).

F. Gygax *et al.*, *J. Less Common Metals* **101**, 97 (1984).

R. Hayano *et al.*, *Phys. Rev. B* **20**, 850 (1979).

E. Holzschuh, *Phys. Rev. B* **27**, 102 (1983).

V. Hughes, *Physica Scripta* **T22**, 111 (1988).

R. Kadono, *Hyperfine Int.* **64**, 615 (1990).

R. Kadono, in "Perspectives of Meson Science", eds. T. Yamazaki, K. Nakai and K. Nagamine 113 (1992).

Y. Kagan and M. Klinger, *J. Phys. C* **7**, 2791 (1974).

Y. Kagan and N. Prokof'ev, *Phys. Lett. A* **150**, 320 (1990).

Y. Kagan and N. Prokof'ev, *Phys. Lett. A* **159**, 289 (1991).

Y. Kagan and N. Prokof'ev, in "Modern Problems in Condensed Matter Science", eds. A.J. Leggett and Yu.M. Kagan (1992).

K. Kehr, G. Honig, and D. Richter, *Z. Phys. B* **32**, 49 (1978).

H. Keller *et al.*, *Phys. Rev. B* **35**, 2008 (1987).

R. Kiefl *et al.*, *Phys. Rev. B* (Rapid Commun.) **34**, 681 (1986).

R. Kiefl *et al.*, Proc. of 15th Int'l Conf. on Defects in Semiconductors, Budapest (1988).

R. Kiefl *et al.*, *Phys. Rev. Lett.* **64**, 2082 (1990).

R. Kiefl and S. Kreitzman, in "Perspectives of Meson Science", eds. T. Yamazaki, K. Nakai and K. Nagamine 265 (1992).

R. Kiefl *et al.*, *Phys. Rev. Lett.* **69**, 2005 (1992).

J. Kondo, *Hyperfine Int.* **31**, 117 (1986).

J. Kondo, in "Perspectives of Meson Science", eds. T. Yamazaki, K. Nakai and K. Nagamine 137 (1992).

S. Kreitzman *et al.*, *Phys. Rev. Lett.* **56**, 181 (1986).

S. Kreitzman, D. Williams, N. Kaplan, and J. K. and J.H. Brewer, *Phys. Rev. Lett.* **61**, 2890 (1988).

S. Kreitzman, *Hyperfine Int.* **65**, 1055 (1990).

R. Kubo and T. Toyabe, in "Magnetic Resonance and Relaxation", ed. R. Blinc 810 (1966).

Y. Kuno *et al.*, *Phys. Lett. B* **148**, 270 (1984).

T. Lee and C. Yang, *Phys. Rev.* **104**, 254 (1956).

T. Lee and C. Yang, *Phys. Rev.* **105**, 1671 (1957).

G. Luke *et al.*, *Phys. Rev. B* **43**, 3284 (1991).

L. Michel, *Proc. Phys. Soc. (London)* **A63**, 514 (1950).

A. Möslang *et al.*, *Phys. Rev. B* **27**, 2674 (1983).

C. Niedermayer *et al.*, *Phys. Rev. Lett.* **71**, 1764 (1993).

K. Nishiyama, in "Perspectives of Meson Science", eds. T. Yamazaki, K. Nakai and K. Nagamine 199 (1992).

B. Patterson, *Rev. Mod. Phys.* **60**, 69 (1988).

P. Percival *et al.*, *Chem. Phys. Lett.* **133**, 465 (1987).

K. Petzinger, *Phys. Rev. B* **26**, 6530 (1982).

H. Primakoff, in *Muon Physics*, Vol. II, "Weak Interactions", ed. V.W. Hughes and C.S. Wu 3 (1975).

F. Rasetti, *Phys. Rev.* **66**, 1 (1944).

T. Riseman and J. Brewer, *Hyperfine Int.* **63**, 249 (1990).

E. Roduner, *Lecture Notes in Chemistry* **49**, (1988).

A. Sachs and A. Sirlin, in *Muon Physics*, Vol. II, "Weak Interactions", ed. V.W. Hughes and C.S. Wu 49 (1975).

J. Schneider *et al.*, *Phys. Rev. B* **41**, 7254 (1990).

J. Schneider *et al.*, *Phys. Rev. Lett.* **68**, 3196 (1992).

A. Seeger and L. Schimmele, in "Perspectives of Meson Science", eds. T. Yamazaki, K. Nakai and K. Nagamine 293 (1992).

P. Stamp and C. Zhang, *Phys. Rev. Lett.* **66**, 1902 (1991).

D. Stoker *et al.*, *Phys. Rev. Lett.* **54**, 1887 (1985).

V. Storchak *et al.*, *Phys. Rev. Lett.* **72**, 3056 (1994).

Y. Uemura *et al.*, *Phys. Rev. Lett.* **62**, 2317 (1989).

Y. Uemura, in "Perspectives of Meson Science", eds. T. Yamazaki, K. Nakai and K. Nagamine 87 (1992).

R. Winston, *Phys. Rev.* **129**, 2766 (1963).

C. Wu, E. Ambler, R. Hayward, and D. H. and R.P. Hudson, *Phys. Rev.* **105**, 1413 (1957).

K. Yamada, A. Sakurai, S. Miyazima, and H. Hwang, *Prog. Theor. Phys.* **75**, 1030 (1986).

H. Yen, M. Sc. thesis, University of British Columbia, (unpublished), (1988).

Further Reading

Several excellent reviews of the *applications* of $\mu\mathcal{SR}$ have been written in recent years; I recommend the book *Muon Spin Rotation Spectroscopy: Principles and Applications in Solid State Physics* by A. Schenck (Adam Hilger, Bristol 1986) and the review article entitled "Implanted Muon Studies in Condensed Matter Science" by S.F.J. Cox in *J. Phys. C: Solid State Phys.* Vol. **20**, pp. 3187-3319 (1987).

The Proceedings of all six International Conferences on $\mu\mathcal{SR}$ to date have been published in *Hyperfine Interactions* as special Volumes **6** (1979), **8** (1981), **17-19** (1984), **31** (1986), **63-65** (1990) and **85-87** (1994). These (and any subsequent Proceedings) are the ideal sources for state-of-the-art developments in $\mu\mathcal{SR}$.